Synaptic oligomeric tau in Alzheimer's disease – a potential culprit in the spread of tau pathology through the brain

Neuron

Article

Synaptic oligomeric tau in Alzheimer's disease — A potential culprit in the spread of tau pathology through the brain

Graphical abstract

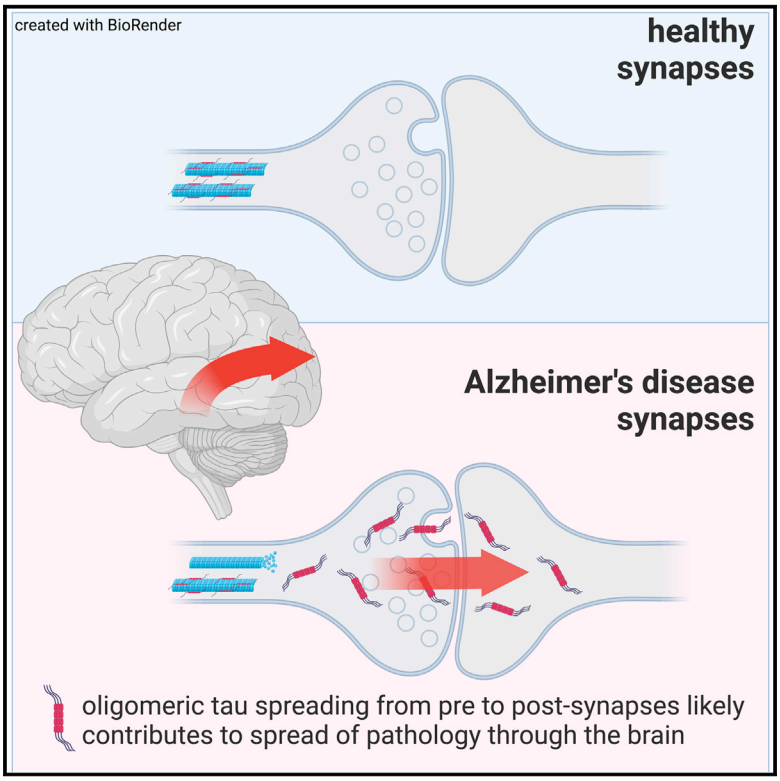

Authors

Martí Colom-Cadena, Caitlin Davies, Sònia Sirisi, ..., Mathew H. Horrocks, Alberto Lleó, Tara L. Spires-Jones

Correspondence

alleo@santpau.cat (A.L.), Tara.spires-jones@ed.ac.uk (T.L.S.-J.)

In brief

Colom-Cadena and colleagues demonstrate using sub-diffraction-limit microscopy that synaptic oligomeric tau is a likely culprit in the spread of tau pathology through the brain in Alzheimer's disease. These data indicate that reducing oligomeric tau at synapses may be a promising therapeutic strategy to stop disease progression.

Highlights

- Oligomeric tau is present in synapses in Alzheimer's disease cortex
- There is more oligomeric tau than phosphorylated or misfolded tau in synapses
- Synaptic oligomeric tau is present even in areas without tangles
- Oligomeric tau spreads from pre to post synapses in a mouse model

Colom-Cadena et al., 2023, Neuron *111*, 1–14
July 19, 2023
https://doi.org/10.1016/j.neuron.2023.04.020

CellPress

Neuron

CellPress
OPEN ACCESS

Article

Synaptic oligomeric tau in Alzheimer's disease — A potential culprit in the spread of tau pathology through the brain

Martí Colom-Cadena,[1,9] Caitlin Davies,[1,9] Sònia Sirisi,[2,3] Ji-Eun Lee,[4,8] Elizabeth M. Simzer,[1] Makis Tzioras,[1] Marta Querol-Vilaseca,[2,3] Érika Sánchez-Aced,[2,3] Ya Yin Chang,[1] Kristjan Holt,[1] Robert I. McGeachan,[1] Jamie Rose,[1] Jane Tulloch,[1] Lewis Wilkins,[1] Colin Smith,[5] Teodora Andrian,[6] Olivia Belbin,[2,3] Sílvia Pujals,[7] Mathew H. Horrocks,[4,8] Alberto Lleó,[2,3,*] and Tara L. Spires-Jones[1,10,*]

[1]The University of Edinburgh Centre for Discovery Brain Sciences and UK Dementia Research Institute, Edinburgh, UK
[2]Memory Unit, Department of Neurology, Institut d'Investigacions Biomèdiques Sant Pau – Hospital de Sant Pau, Universitat Autònoma de Barcelona, Barcelona, Spain
[3]Centro de Investigación Biomédica en Red en Enfermedades Neurodegenerativas (CIBERNED), Madrid, Spain
[4]EaStCHEM School of Chemistry, The University of Edinburgh, Edinburgh, UK
[5]Centre for Clinical Brain Sciences and Sudden Death Brain Bank, The University of Edinburgh, Edinburgh, UK
[6]Nanoscopy for Nanomedicine Lab, Institute of Bioengineering of Catalonia (IBEC Barcelona Institute of Science and Technology), Barcelona, Spain
[7]Department of Biological Chemistry, Institute for Advanced Chemistry of Catalonia (IQAC-CSIC), Barcelona, Spain
[8]IRR Chemistry Hub, Institute for Regeneration and Repair, The University of Edinburgh, EH16 4 UU Edinburgh, UK
[9]These authors contributed equally
[10]Lead contact
*Correspondence: alleo@santpau.cat (A.L.), Tara.spires-jones@ed.ac.uk (T.L.S.-J.)
https://doi.org/10.1016/j.neuron.2023.04.020

SUMMARY

In Alzheimer's disease, fibrillar tau pathology accumulates and spreads through the brain and synapses are lost. Evidence from mouse models indicates that tau spreads *trans*-synaptically from pre- to postsynapses and that oligomeric tau is synaptotoxic, but data on synaptic tau in human brain are scarce. Here we used sub-diffraction-limit microscopy to study synaptic tau accumulation in postmortem temporal and occipital cortices of human Alzheimer's and control donors. Oligomeric tau is present in pre- and postsynaptic terminals, even in areas without abundant fibrillar tau deposition. Furthermore, there is a higher proportion of oligomeric tau compared with phosphorylated or misfolded tau found at synaptic terminals. These data suggest that accumulation of oligomeric tau in synapses is an early event in pathogenesis and that tau pathology may progress through the brain via *trans*-synaptic spread in human disease. Thus, specifically reducing oligomeric tau at synapses may be a promising therapeutic strategy for Alzheimer's disease.

INTRODUCTION

Of the neuropathological hallmarks of Alzheimer's disease (AD), synapse loss is the strongest correlate of cognitive decline,[1–3] and progression of tau pathology through the AD brain closely correlates with synaptic loss and cognitive symptoms.[4,5] Tau protein binds synaptic vesicles and is thought to have physiological roles in synapses.[6] In animal and neuronal culture model systems, accumulation of hyperphosphorylated and misfolded tau within synapses causes synaptic dysfunction and synapse loss.[7–13]

While neurofibrillary tangles (NFTs) were historically considered neurotoxic lesions, data over the past decades indicate that the tau fibrils in tangles are relatively inert and that soluble oligomeric forms of tau are more toxic to synapses and neurons in mouse models of tauopathy.[14,15] Much less is known about synaptic tau and in particular synaptic oligomers in human brain, which is an important knowledge gap to address in order to develop tau-directed therapeutics to protect synapses from degeneration. Phosphorylated and misfolded tau have previously been observed in human AD synapses using biochemical and imaging methods.[12,16,17] There is a small amount of evidence from human cases suggesting that diffuse forms of tau precede NFT formation,[18,19] that those diffuse forms are mainly oligomeric species,[20,21] and that oligomeric tau is important for seeding activity.[22] Both high seeding activity and high concentrations of oligomers have been linked to worse cognitive outcomes.[22,23]

Please cite this article in press as: Colom-Cadena et al., Synaptic oligomeric tau in Alzheimer's disease — A potential culprit in the spread of tau pathology through the brain, Neuron (2023), https://doi.org/10.1016/j.neuron.2023.04.020

Table 1. Demographic, neuropathological, and genetic characteristics of human subjects

BBN	SSD	Clinical diagnosis	*APOE* genotype	Age (years)	Sex	PMI (h)	Brain weight (g)	Brain pH	Braak stage	Thal phase	Study
BBN_19686	SD063/13	control	3/3	77	F	75	1320	6.5	I	I	1,9
001.26495	SD024/15	control	3/3	78	M	39	1290	6.17	I	0	1,2,5,7,8,9
001.28402	SD051/15	control	3/3	79	M	49	1503	6.33	I	2	1
001.28406	SD001/16	control	3/3	79	M	72	1437	6.13	II	2	1,2,5,6,7,8,9
001.28793	SD017/16	control	3/3	79	F	72	1219	5.95	II	1	1,2,5,6,7,8,9
001.28797	SD025/16	control	3/3	79	M	57	1301	6.11	0	0	1,2,5,6,7,8
001.32577	SD002/18	control	3/3	81	M	74	1313	6.07	II	3	1
001.35215	SD008/19	control	3/3	82	M	40	1246	6.01	I	NA	1
001.35549	SD030/19	control	3/3	82	M	56	1326	6.01	I	1	1
001.29082	SD031/16	control	3/4	79	F	80	1339	5.96	III	5	1,2,5,6,7,8
001.34131	SD029/18	control	3/4	82	M	95	1472	5.97	IV	3	1,2,5,6,7,8,9
001.35181	SD003/19	control	3/4	82	M	49	1,496	6.12	II	2	1,2,5,6,7,8,9
001.28794	SD018/16	control	2/3	79	F	61	1,289	5.76	I	0	2,5,7,8,9
001.29086	SD034/16	control	3/3	79	F	68	1,468	6.2	0	1	2,5,6,7,8,9
001.35866	SD046/19	control	NA	83	F	78	1,158	5.96	IV	4	2,5,6,7,8,9
001.36435	SD013/21	control	3/3	84	M	95	1,222	6.00	II	1	3
001.35511	SD025/19	control	2/3	86	M	123	1,553	6.17	II	1	3
001.36135	SD012/20	control	3/3	84	F	30	1,214	5.93	II	1	3
001.36809	SD023/21	control	3/3	85	M	3	1,400	6.10	II	1	3
BBN_24527	SD056/14	AD	3/3	81	M	74	1,160	6.1	V	4	1,2,5,6,7,8,9
001.28410	SD005/16	AD	3/3	62	F	109	1,029	6.04	VI	5	1
001.28771	SD010/16	AD	3/3	85	M	91	1,183	5.95	VI	5	1,2,5,6,7,8,9
001.29081	SD030/16	AD	2/3	90	F	110	943	6.06	VI	5	1
001.32929	SD012/18	AD	3/3	85	F	80	1,354	6.03	VI	5	1,2,5,6,7,8,9
001.35182	SD004/19	AD	3/3	66	M	49	1,225	6.12	VI	5	1,9
BBN_24322	SD049/14	AD	3/4	80	M	101	1,410	6.10	VI	5	1,2,5,7,8
BBN_24526	SD055/14	AD	3/4	79	M	65	1,300	6.05	VI	NA	1
BBN_24668	SD058/14	AD	3/4	96	F	61	1,082	6.11	VI	NA	1
BBN_25739	SD014/15	AD	3/4	85	F	45	1,375	5.77	VI	5	1,2,5,6,7,8,9
001.26718	SD040/15	AD	3/4	78	M	74	1,367	6.13	VI	5	1,2,5,6,7,8,9
001.29135	SD027/16	AD	3/4	90	M	73	1,275	6.44	VI	3	1
001.29521	SD035/16	AD	3/4	95	M	96	1,221	6.08	VI	5	1
001.29695	SD004/17	AD	3/4	86	M	72	1,300	6.1	VI	5	1,2,5,7,8,9
001.30142	SD020/17	AD	3/4	88	F	112	1,054	5.96	VI	5	1,2,5,6,7,8,9
001.30883	SD034/17	AD	3/4	61	F	69	1,060	6.15	VI	5	1
001.30973	SD039/17	AD	3/4	89	F	96	1,210	6.03	VI	5	1,2,5,6,7,8,9
001.33636	SD017/18	AD	3/4	93	M	43	1,117	5.92	VI	5	1
001.35096	SD037/18	AD	3/4	72	M	103	1,209	6.18	VI	5	1,2,5,6,7,8
001.35535	SD028/19	AD	3/4	83	F	95	1,400	6.55	VI	4	1
001.35564	SD031/19	AD	3/4	90	F	52	1,075	5.99	VI	5	3
001.36297	SD022/20	AD	3/4	84	M	87	1,163	5.82	VI	5	3
001.36346	SD027/20	AD	NA	90	F	60	932	6.1	VI	5	3
		AD	NA	90	F	18	1,110	NA	V	5	4

AD, Alzheimer's disease; APOE, Apolipoprotein E; BBN, Medical Research Council Brain Bank number; SD, Sudden Death Brain Bank number; NA, not available; PMI, postmortem interval. Study number as included in Table S1.

Please cite this article in press as: Colom-Cadena et al., Synaptic oligomeric tau in Alzheimer's disease — A potential culprit in the spread of tau pathology through the brain, Neuron (2023), https://doi.org/10.1016/j.neuron.2023.04.020

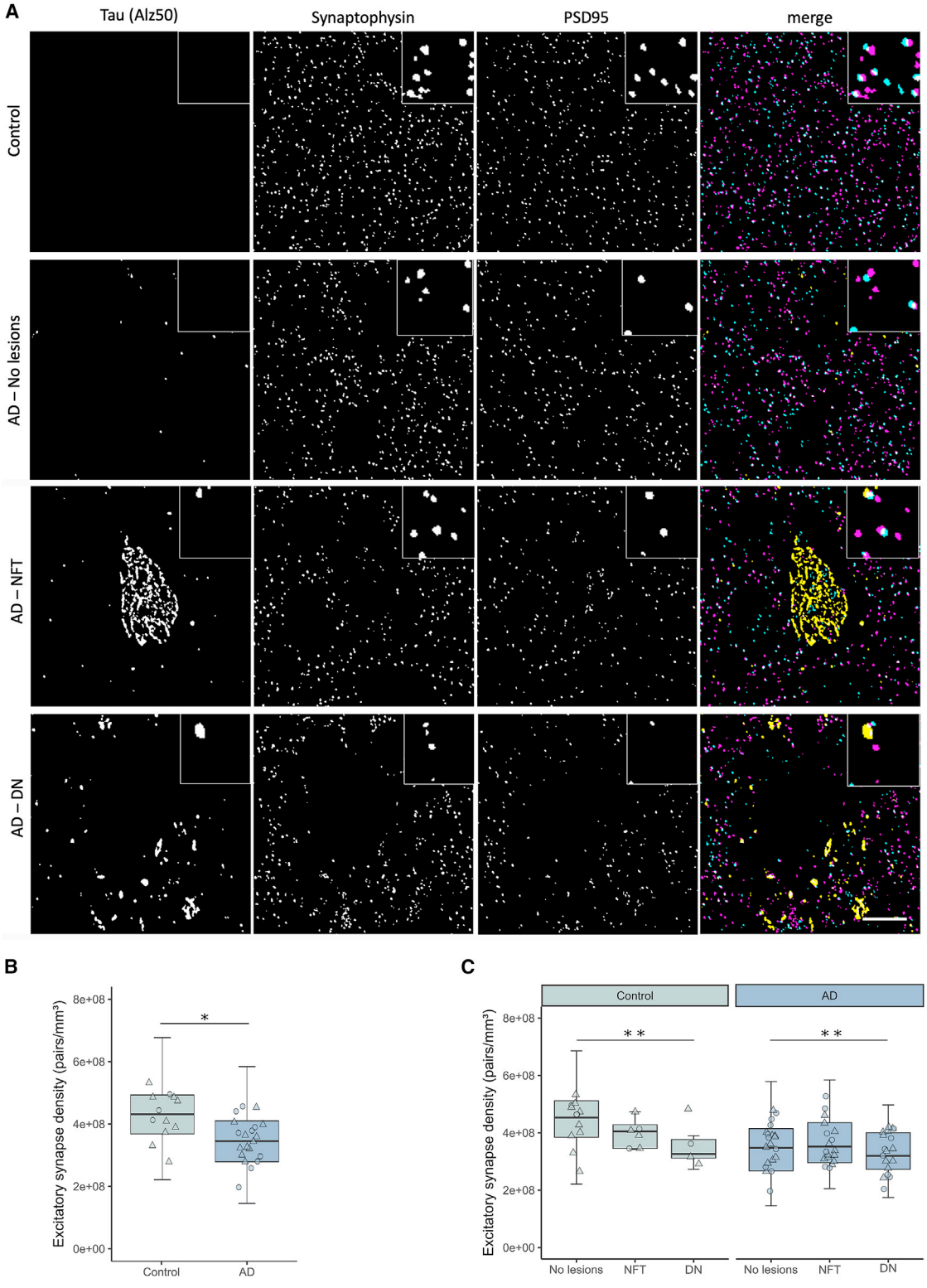

(legend on next page)

Please cite this article in press as: Colom-Cadena et al., Synaptic oligomeric tau in Alzheimer's disease — A potential culprit in the spread of tau pathology through the brain, Neuron (2023), https://doi.org/10.1016/j.neuron.2023.04.020

In addition to synaptotoxic effects, synaptic localization of tau is potentially important for propagation of tau pathology through brain networks. Seminal observations of the patterns of tau pathology postmortem by Braak and Braak[24] and more recent observations using tau ligands for positron emission tomography (PET)[25,26] demonstrate that NFTs accumulate in a stereotypical spatiotemporal sequence beginning in the brain stem and *trans*-entorhinal cortex and progressing through synaptically connected neural circuits. Because tau is secreted by presynaptic terminals in an activity-dependent manner[27] and misfolded tau can act as a seed to initiate pathological changes in naive tau *in vitro* and *in vivo,*[28,29] a likely method of pathological propagation is via synaptic connections. It is also possible that anatomically connected brain regions are sequentially vulnerable to tau. A recent analysis of tau PET imaging and postmortem data indicates that local replication, rather than spreading between brain regions, may be more closely related to regional tau pathology.[30] These two ideas are not mutually exclusive, and indeed the local accumulation of tau may at least partially reflect *trans*-synaptic spread in local circuits, which one might predict would occur faster because of the shorter axons of local connections.

We and others have previously demonstrated *trans*-synaptic tau spread in model systems including transgenic mice expressing human tau in the entorhinal cortex and viral-mediated tau expression.[31–35] These studies prove that *trans*-synaptic tau spread is biologically possible. However, one limitation is that it might have been artificially induced by overexpression in models, and this phenomenon has not been conclusively demonstrated in human brain. Here, we use sub-diffraction-limit optical imaging of synapses with multiple techniques and multiple tau antibodies (detecting oligomeric, misfolded, and phosphorylated tau) to explore in human postmortem brain whether there is evidence of tau present in both the pre- and postsynaptic sides of the same synapses, which could be due to *trans*-synaptic spread. Furthermore, we characterize tau pathology in detail to determine whether synaptic tau accumulates in areas without substantial NFTs.

RESULTS

Excitatory synapses are lost in Alzheimer's disease

Using human postmortem brain samples prepared for array tomography (Table 1), we first replicated the observations from previous studies where synapse loss has been observed in AD.[1–3,36,37] Using array tomography, we imaged 1,315,583 individual excitatory synaptic pairs in inferior temporal cortex (BA20/21). Synaptic pairs were defined as a synaptophysin-positive presynaptic puncta with a PSD95 puncta within 0.5 μm (distance between centroids). This distance was chosen based on electron microscopy data and analysis of synaptic pairs in this array tomography dataset with differing cut-off distances (Figures S1A and S1B). We observed a 1.25-fold decrease in excitatory synapse density in AD when compared to controls (Control median = $4.29 \times 10^8 \pm 7.49 \times 10^7$ [n = 12]; AD median = $3.45 \times 10^8 \pm 9.99 \times 10^7$ [n = 20]; $\beta = -5{,}314.01$; $p = 0.023$; Figures 1A and 1B). Next, we investigated the relationship between pathological aggregates and synaptic loss in the immediate environment. To do this, regions of interest were chosen at 63× magnification with either a neurofibrillary tangle, neuritic plaque, or no aggregate in the center of the field of view (140.6 × 106.6 μm area; Figure S1C). A decrease in synapse density was observed around clumps of dystrophic neurites (DNs) containing tau that surround amyloid aggregates in neuritic plaques (Control $\beta = 3{,}862$; $p = 0.005$; AD $\beta = 3{,}862$; $p = 0.005$[37,38]). In contrast to DNs, the presence of NFTs was not associated with a decreased number of excitatory synapses in the immediate environment (Figures 1A and 1C).

Oligomeric, misfolded, and phosphorylated tau species accumulate in postsynaptic terminals of AD cases

We next investigated the presence of tau at postsynaptic terminals. Three species of tau were studied: oligomeric (T22 antibody, characterized by Lasagna-Reeves[21]), misfolded (Alz50 antibody), and Ser202, Thr205 phosphorylated (AT8 antibody) (Figures 2A–2E and S2A–S2I). All three tau species were found in postsynaptic terminals of AD cases, with a higher presence of oligomeric tau stained with T22 than the other markers (Figure 2F). Control cases also had a small amount of postsynaptic tau pathology. Interestingly, T22 and AT8 were often found in the same postsynapses, while Alz50 was largely found in different synapses of AD cases (Figure 2G). There was a stronger correlation between postsynaptic tau species in AD than control cases (Figure 2G).

PSD95 puncta size did not differ between control and AD cases (Figure S2J). However, there were differences in PSD95 volume when tau species were present (ANOVA after linear mixed effects model $F[3,102.3] = 6.85$, $p < 0.001$). All tau species had a tendency to colocalize with bigger postsynaptic terminals, with T22 being the highest observed increase, especially in control cases. We observed similar results when looking at PSD95 signal intensity as a proxy for protein levels. When looking at all postsynaptic terminals, signal intensity did not differ between control and AD cases (Figure S2K). Again, there were differences when looking at the presence of different tau species and signal intensity (ANOVA after linear mixed effects model $F[3,98.3] = 8.97$, $p < 0.001$). There was an overall increase of postsynaptic intensity when each tau species was present, with T22 being the highest

Figure 1. Excitatory synapse loss in BA20/21 of AD cases and its relationship to hallmark tau aggregates

(A) Representative single 70-nm-thick segmented images of a control case and AD cases with no hallmark tau aggregates (AD-no lesions), a neurofibrillary tangle (AD-NFT), or dystrophic neurite clumps around neuritic plaques (AD-DN). In merged composite images, synaptophysin presynaptic terminals are shown in magenta, PSD95 postsynaptic terminals in cyan, and misfolded tau (Alz50) in yellow.

(B) Excitatory synapse density was decreased in AD cases when compared to controls.

(C) The quantification of synaptic terminals split by the presence of tau aggregates. Boxplots show quartiles and medians calculated from each image stack. Data points refer to case means (females, circles; males, triangles). Analysis was with linear mixed effects models, including diagnostic group, sex, and pathology in the image (no effect of sex). Scale bar represents 10 μm. Insets, 5 × 5 μm. NFT, neurofibrillary tangle; DN, dystrophic neurite. *$p < 0.05$, **$p < 0.01$. See also Figure S1 and Table S1.

Please cite this article in press as: Colom-Cadena et al., Synaptic oligomeric tau in Alzheimer's disease — A potential culprit in the spread of tau pathology through the brain, Neuron (2023), https://doi.org/10.1016/j.neuron.2023.04.020

CellPress
OPEN ACCESS

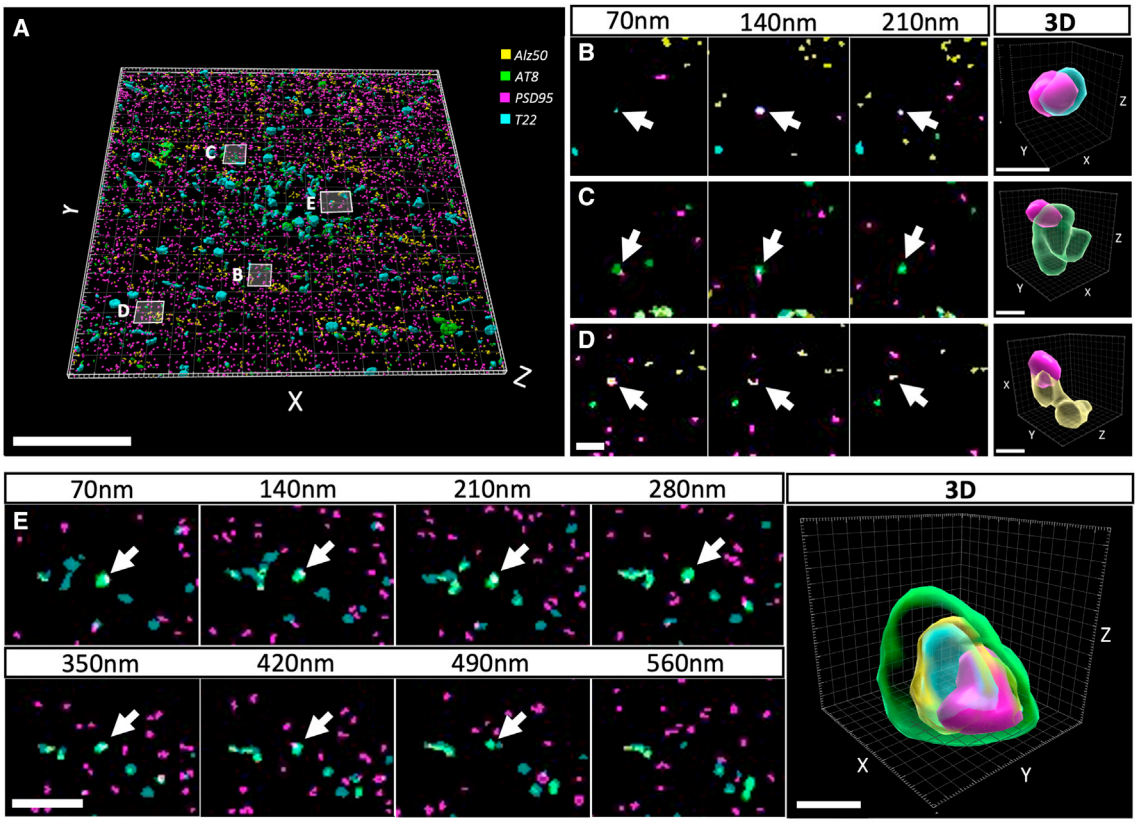

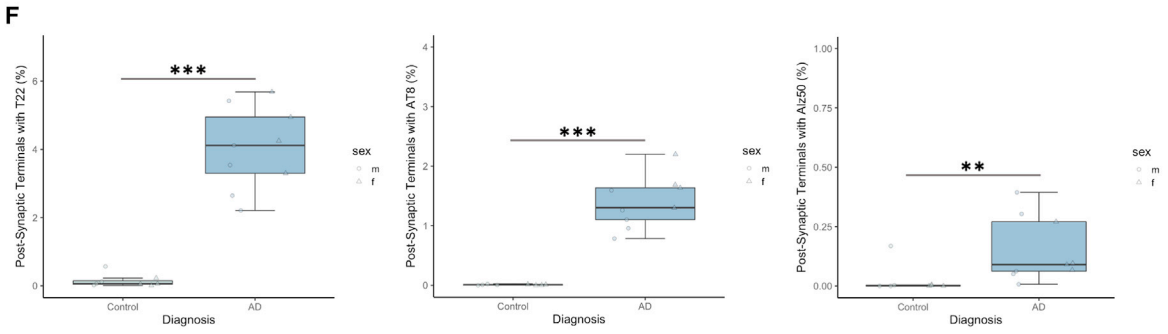

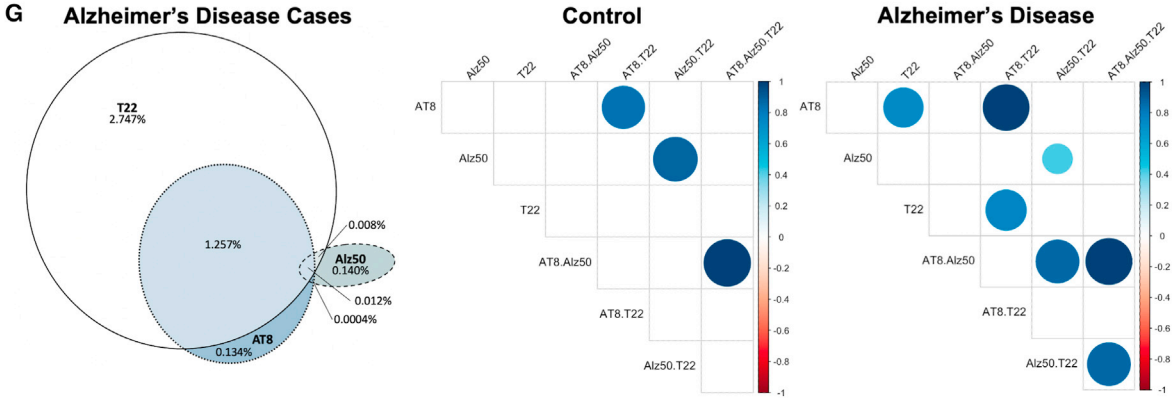

(legend on next page)

Please cite this article in press as: Colom-Cadena et al., Synaptic oligomeric tau in Alzheimer's disease — A potential culprit in the spread of tau pathology through the brain, Neuron (2023), https://doi.org/10.1016/j.neuron.2023.04.020

observed increase in control cases. Taken together, both the PSD95 size and signal intensity seem to be related to the presence of tau species, with oligomeric tau (T22) associated with the highest increases.

The presence of tau at the synapses was confirmed with other high-resolution techniques. Immunogold electron microscopy was performed in 4 control and 3 AD cases. In all cases, we observe T22-positive globular-appearing oligomers associated with fibrils in neurofibrillary tangles and on fibrils in neurites. T22 immunogold staining is also observed on presynaptic vesicles and in postsynaptic terminals near the postsynaptic density (Figures 3A and S3A). Synaptic accumulation of tau was also confirmed with direct stochastic optical reconstruction microscopy (dSTORM, 1 control case and 1 AD case) (Figures 3B and S3D) and DNA points accumulation for imaging in nanoscale topography (DNA-PAINT) in an AD case (Figures 3B and S3C). Together these super-resolution imaging techniques conclusively show pathological tau in pre- and postsynaptic terminals. Finally, the presence of oligomeric tau was biochemically confirmed with western blot of synaptoneurosome preparations from AD (n = 8) and control (n = 8) cases (Figures 3C and S3B).

Synaptic oligomeric tau precedes the presence of neurofibrillary tangles

To determine whether oligomeric tau accumulation in synapses is an early pathological event, we next investigated the regional relationship between the presence of NFTs and the synaptic accumulation of oligomeric tau.

Temporal cortex (BA20/21) and primary visual cortex (BA17) samples from 10 AD cases and 10 controls were investigated for the presence of oligomeric tau at synaptic terminals by array tomography microscopy and for the presence of NFTs in larger fields of view by immunohistochemistry (IHC) on paraffin sections from the same cases and brain regions (Figure 4A). We found that in areas with no or low NFT counts, there was already oligomeric tau accumulating at presynaptic terminals both in control and in AD cases (Figures 4A and 4B). There was a positive correlation between NFTs and the total amount of oligomeric tau, especially in brain areas highly affected by tau pathology (AD cases at BA20/21; $R = 0.81$, $p = 0.022$; Figure 4C). However, the proportion of oligomeric tau at synaptic terminals was lower when more total oligomeric tau was present, especially in BA17, where there is less overt tau pathology (AD cases at BA17; $R = -0.87$, $p = 0.0027$; Figure 4D).

To confirm whether synaptic oligomeric tau is an early phenotype, we compared staining of AT180, which labels tau phosphorylated at residue 231 (reported to be an early marker of tau pathology[39]), with oligomeric tau in synapses. While both types of tau are more prevalent in AD than control synapses, we observe 3.3-fold more T22- than AT180-labeled presynaptic terminals in BA20/21 of AD cases (Presynaptic terminals with T22: control median = 0.297 ± 2.038% [n = 9]; AD median = 5.061 ± 3.389% [n = 9]; $\beta = 4.15$; $p = 0.004$; Figure S4B. Presynaptic terminals with AT180: control median = 0.0219 ± 0.697% [n = 9]; AD median = 1.534 ± 1.441% [n = 9]; $\beta = 1.537$; $p = 0.01$; Figure S4C).

Indirect evidence of transsynaptic transmission of tau aggregates

The finding of tau accumulating at synapses of AD cases even in areas with little tau pathology is in line with the hypothesis that tau may spread *trans*-synaptically. To further explore this possibility, the subset of tau-containing excitatory synaptic pairs was explored for pre- and postsynaptic locations of tau (Figure 5A). Oligomeric tau was differentially located in the synaptic compartments (ANOVA after linear mixed effects model $F[2,88] = 73.61$, $p < 0.0001$); it was more commonly found in presynaptic terminals only, with a gradient toward postsynaptic localization (Figure 5B). In inferior temporal cortex, BA20/21, we confirmed that misfolded tau antibody (Alz50) was also found in both sides of the synapse (Figures S5A–S5E). Finally, to overcome the descriptive nature of postmortem studies, we investigated transsynaptic spreading of oligomeric tau in an animal model. We previously demonstrated that human tau can spread from pre- to postsynaptic terminals in a mouse model with overexpression of human P301L mutant tau and synaptophysin tagged with GFP in entorhinal cortex.[34] Here, tissue from this same mouse model was stained with T22 to show that oligomeric tau can spread from pre- to postsynaptic terminals in mammalian brain (Figure S5F).

DISCUSSION

In the present work, we show that oligomeric, phosphorylated, and misfolded tau can be detected within synapses of human AD cases. As far as we know, this study represents the first comprehensive visualization of oligomeric tau at synaptic terminals in human tissue. The presence of oligomeric tau at synaptic terminals was observed even in cases with low NFT pathology and represented a higher proportion of the tau burden in regions with little NFT pathology, suggesting an early synaptic localization of oligomeric tau. The distribution of oligomeric tau at synapses was asymmetric, with the highest proportion in

Figure 2. Different tau species accumulate in postsynaptic terminals

(A) An aligned and segmented three-dimensional image stack from an AD case stained for oligomeric tau (T22, cyan), misfolded tau (Alz50, yellow), Ser202, Thr205 phosphorylated tau (AT8, green), and postsynaptic densities (PSD95, magenta).

(B–E) All three types of tau can be observed in postsynapses, as shown in serial sections and three-dimensional reconstructions of individual synapses (B–E).

(F) Quantification (F) reveals increases in synaptic terminals containing tau in AD compared to control. Boxplots show quartiles and medians calculated from each image stack. Data points refer to case means (females, circles; males, triangles). ***$p < 0.001$, **$p < 0.01$.

(G) A Venn diagram of the percentage of synapses that contain tau staining in AD cases (G, left) reveals that T22 is found in more synapses than the other species and that it colocalizes often with AT8. Alz50 colocalizes less with the other species. Correlation plots (G, right) show differences ($p < 0.01$) between markers in control and AD cases. For example, synaptic T22 correlates with synaptic AT8 in AD but not in control cases. Scale bars represent 20 μm in (A), 2 μm in left panels of (B)–(E), and 0.5 μm in 3D reconstructions in (B)–(E). See also Figure S2.

Please cite this article in press as: Colom-Cadena et al., Synaptic oligomeric tau in Alzheimer's disease — A potential culprit in the spread of tau pathology through the brain, Neuron (2023), https://doi.org/10.1016/j.neuron.2023.04.020

CellPress
OPEN ACCESS

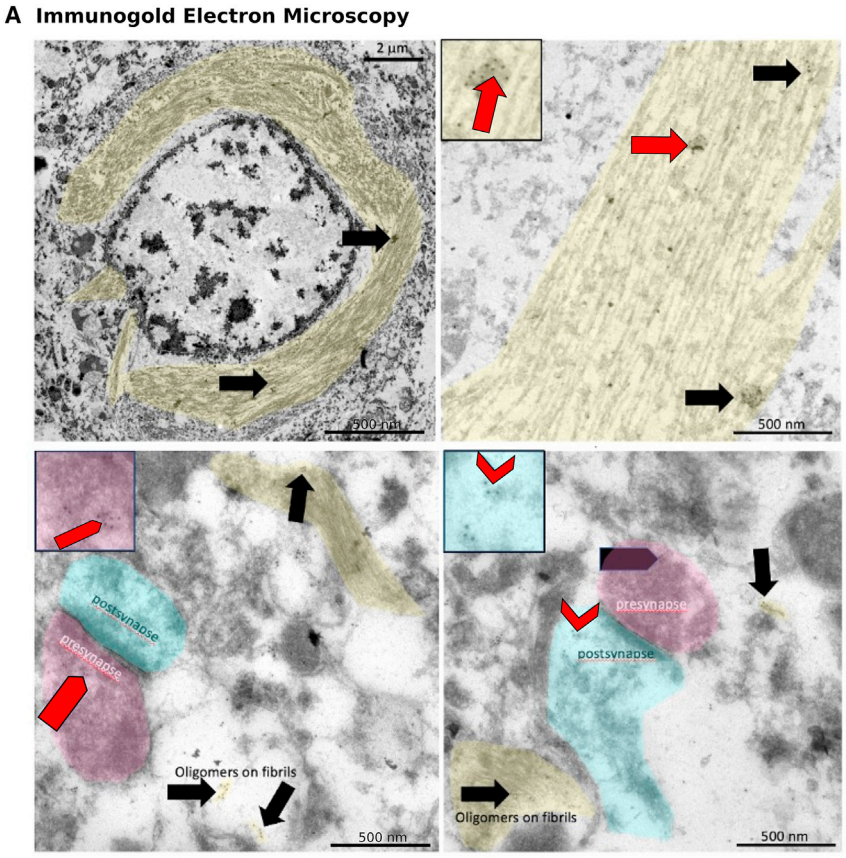

Figure 3. Confirmation of AD synaptic tau aggregates

(A) Immunoelectron microscopy with gold-conjugated secondary antibodies (black dots) shows T22 labels globular-appearing oligomers associated with fibrils (arrows) in neurofibrillary tangles and on fibrils in neurites (shaded yellow). T22 immunogold staining is also observed on presynaptic vesicles (pentagons, presynapses shaded magenta) and in postsynaptic terminals near the postsynaptic density (chevrons, postsynapses shaded cyan).

(B) dSTORM and DNA-PAINT were used on array tomography sections to confirm tau (yellow) and synaptophysin (magenta) or PSD95 (cyan) colocalization.

(C) Full western blot from synaptoneurosomes isolated from control or AD cases is shown at left and the quantification of oligomeric and/or monomeric bands at right. Boxplots show quartiles and medians (females, triangles; males, circles). *$p < 0.05$. C, control; SAD, Alzheimer's disease. Scale bars EM: 500 nm (insets 250 × 250 nm), dSTORM: 100 nm, DNA-PAINT: 200 nm. See also Figure S3.

A

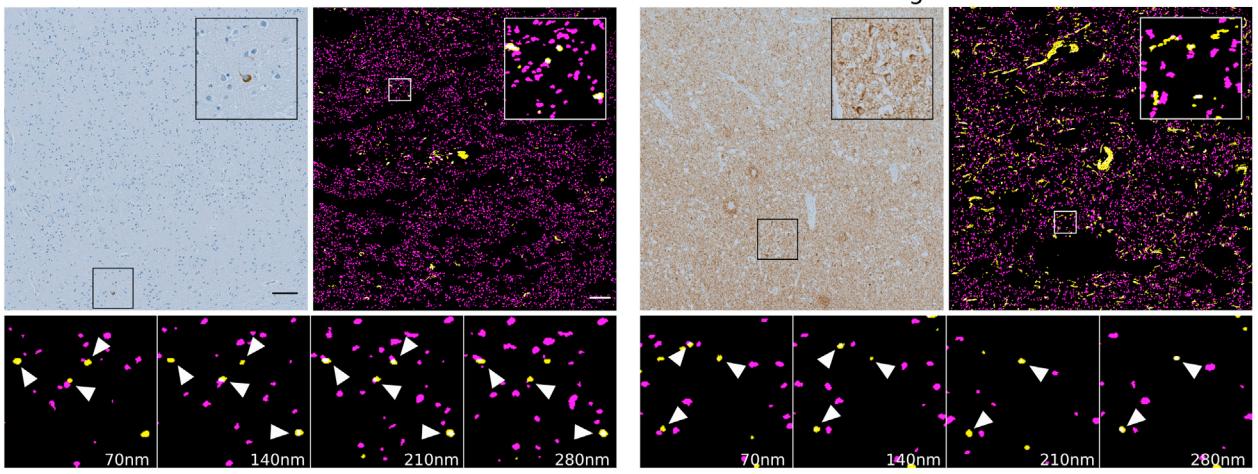

B

Braak NFT stage	BA20/21 Presynaptic terminals with T22 (%)	BA20/21 NFTs per mm²	BA17 Presynaptic terminals with T22 (%)	BA17 NFTs per mm²
0-IV	0.023	0	0.018	0
	0.125	0	0.038	0
	0.573	0	0	0
	0	0.090	0.023	0
	0	0	0	0
	0.135	0	0.018	0.100
V-VI	3.163	0.610	0.055	0.230
	3.905	0.630	1.360	0.030
	5.693	4.690	4.413	0.440
	8.080	6.330	1.198	3.310
	8.345	7.070	0.110	4.010
	11.723	10.090	8.953	10.260
	13.170	12.670	3.495	6.380
	11.198	2.190	0.220	2.320

C

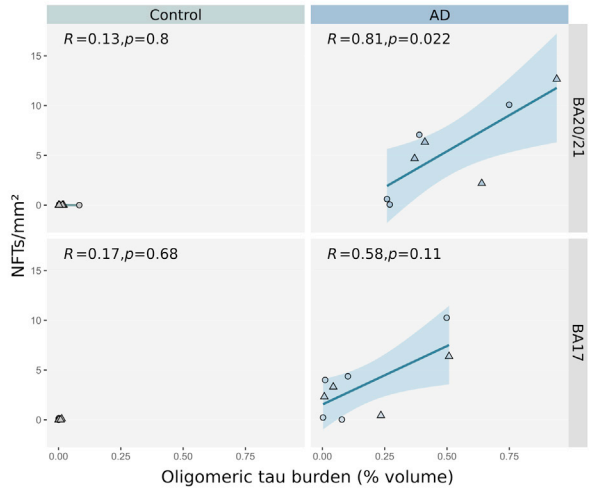

D

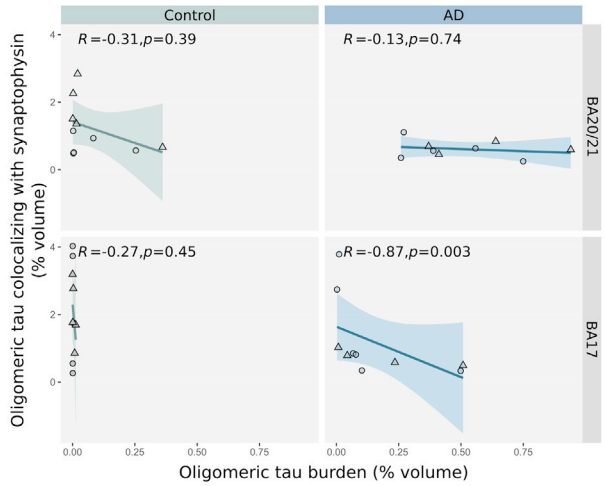

(legend on next page)

presynapses and a gradient toward the postsynapse. This is indirect evidence for transsynaptic anterograde transmission of tau.

Synaptic loss and synaptic tau

Synaptic loss and alterations in synaptic markers represent two of the earliest findings in AD-affected brain regions and are the best pathological correlates of cognitive decline.[2,40,41] Here, we used array tomography microscopy,[42,43] immunogold-electron microscopy, dSTORM, and DNA-PAINT, which allowed us to resolve different tau species in single synaptic terminals.

With this approach, we first replicated the synaptic loss associated with AD, as we and others have shown with several techniques.[36,37,41] Previous studies using array tomography in human postmortem brain identified synapse loss in areas surrounding amyloid-β (Aβ) plaques, with synapse loss correlating with distance from the plaque.[36,37] In this study, paired presynaptic and postsynaptic terminals were reduced in AD and further reduced near neuritic plaques identified by surrounding dystrophic neurites. In contrast, we did not observe synapse loss in the direct vicinity of neurofibrillary tangles. While amyloid plaques are extracellular lesions surrounded by oligomeric Aβ that is known to be toxic to synapses, neurofibrillary tangles are intracellular lesions that are thought to be harmful to the neuron containing them or to reflect a sequestering of toxic tau. This toxicity could induce loss of synapses formed by the tangle-bearing neuron, which are typically distant from the cell body, even in the opposite hemisphere. Some of the postsynaptic dendritic spines of tangle-bearing neurons are likely within the same image stack as the soma, but many of these will also be out of frame. We thus postulate that while plaques cause local synaptic toxicity, tau-induced synaptotoxicity is more diffuse throughout the brain. Second, we found that oligomeric, phosphorylated, and misfolded tau all accumulate in synaptic terminals. We observed an increase in signal intensity and volume in tau-containing postsynaptic terminals, which may reflect compensation for the injured environment, something that has been suggested previously by others.[40,44] However, we need to be cautious interpreting these data, as light microscopy techniques are sensitive, and subtle changes may affect both size and intensity. We have previously observed synaptic tau with antibodies raised to total tau, misfolded tau (Alz50), and tau phosphorylated at serine 202 and threonine 205 (AT8).[11–13] Here, we combined them and found that oligomeric tau is the most common tau species in postsynapses. This is an important finding, as animal studies indicate oligomeric tau is particularly synaptotoxic.[15] In previous postmortem studies, analysis of synaptosomes[45–49] and synaptic fractions of homogenized tissue[50] have identified tau to be localized to both synaptic compartments in control and AD tissue. However, methods involving biochemical isolation of synapses fail to consider the overall architecture of the intact tissue and may unwittingly select for certain populations of synapses. Tissue homogenization can also be damaging to synapses, allowing soluble proteins to leak in or out of the preparations. Further, this method does not generally allow for study of multiple proteins within the same synapse. Array tomography overcomes some of these limitations, offering a means for high-resolution characterization of a large number of synapses *in situ* in human postmortem tissue, and enables the assessment of synaptic density and protein composition.[42]

The oligomeric tau we detected with immunoelectron microscopy is remarkably similar in morphology to oligomers biochemically isolated from human AD extracellular vesicles observed by atomic force microscopy.[51] Here we demonstrate that globular structures containing oligomeric tau are associated with fibrils and within some synapses. We also observe tau labeling of synaptic vesicles consistent with observations in *Drosophila* that tau binds synaptic vesicle proteins and with our previous work showing with array tomography that tau is present in presynaptic terminals.[12,13] This finding was further confirmed with dSTORM and DNA-PAINT, which both demonstrated colocalization between pathological tau and presynaptic vesicle proteins with nanoscale resolution.

The finding of tau, especially oligomeric tau, accumulating at synapses may have implications for the understanding of AD pathogenesis. While many studies have focused on Aβ as the trigger for AD-related synaptic damage, tau can mediate synapse loss, both alone and in concert with Aβ.[52] Most tauopathy models show synapse dysfunction and loss.[7,53–55] And mounting evidence suggests that oligomeric, misfolded forms of tau mediate synaptotoxicity. Tau oligomers may induce morphological changes, impair plasticity, and dysregulate synaptic transmission.[56–59] Oligomers also induce synapse loss and impairment in memory function, which is rescued upon reduction of oligomer levels.[60–62] Thus, at the synapse, tau oligomers may reduce synaptic proteins, alter neuronal signaling, promote synapse loss and impair memory function.

In this study, we also found oligomeric tau in cases with no or low NFT presence. These findings are in line with evidence from human cases suggesting that diffuse and neuropil forms of tau precede NFT formation[18,39] and may involve oligomeric species.[20,21] This early (according to NFT burden and the well-established Braak staging) oligomeric tau was found to accumulate at synapses. The seeding activity of tau in synaptoneurosome preparations has also been found to precede the amount of hallmark pathology, as reflected by Braak stages,[63] and seeding closely correlated with

Figure 4. Synaptic oligomeric tau precedes the presence of neurofibrillary tangles

(A) Representative image of a case with spare (left panel) and high (right panel) NFT density. Top left images show tau AT8 immunoreactivity by immunohistochemistry and the inset highlights the presence of NFTs. At top right is a maximum-intensity projection of 12 consecutive 70-nm-thick sections by array tomography microscopy. Presynaptic synaptophysin-positive terminals (magenta) and oligomeric tau (T22, yellow) are shown. The inset highlights the presence of presynaptic terminals with oligomeric tau that are pointed by arrowheads in the horizontal panel of four consecutive 70-nm-thick sections.

(B) Table displaying the density of synaptic terminals that contained oligomeric tau and the NFT density per case, area, and Braak NFT stage. Highlighted in purple are the cases shown in (A).

(C and D) (C) Correlation plots between the density of NFTs and the percent volume of the image occupied by T22 and (D) correlation plots between the percent of T22 that colocalizes with presynaptic terminals and the total amount of T22. Spearman correlation results are shown in each condition. Data points refer to case means (females, circles; males, triangles). Scale bars: left, 100 μm; right, 10μm. Inset sizes: left, 160 × 160 μm; right, 10 × 10 μm. See also Figure S4.

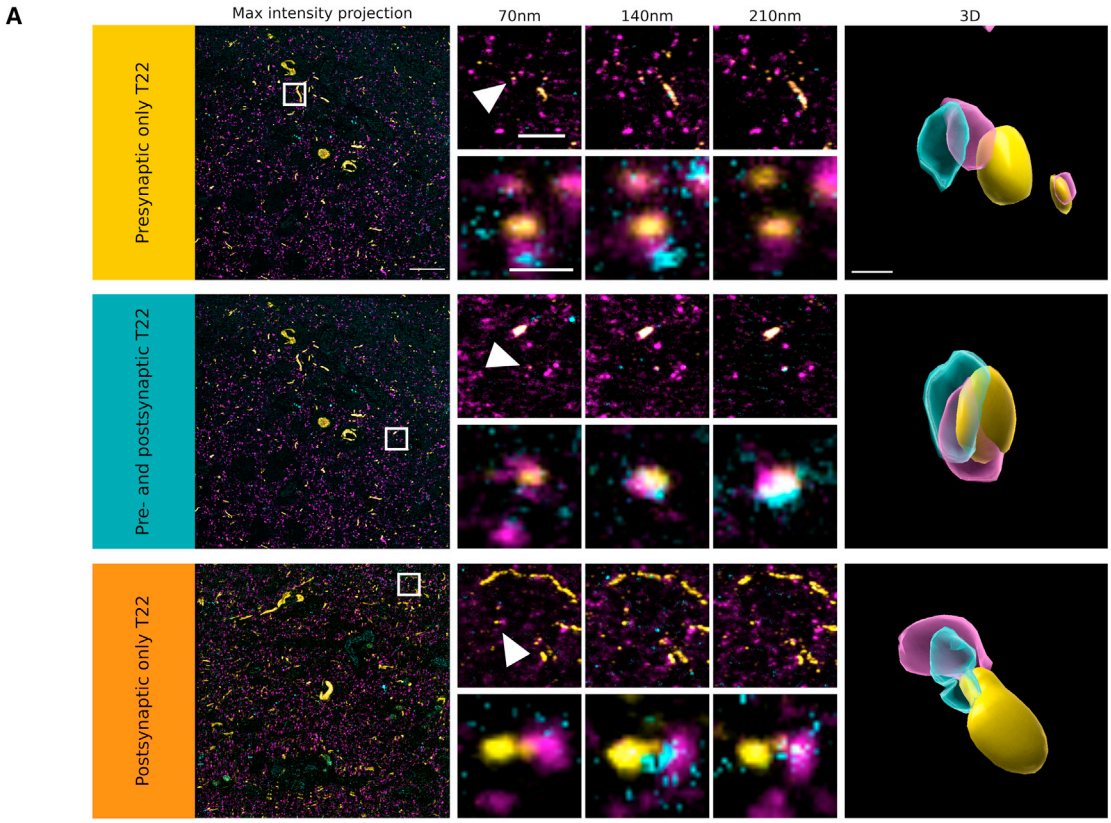

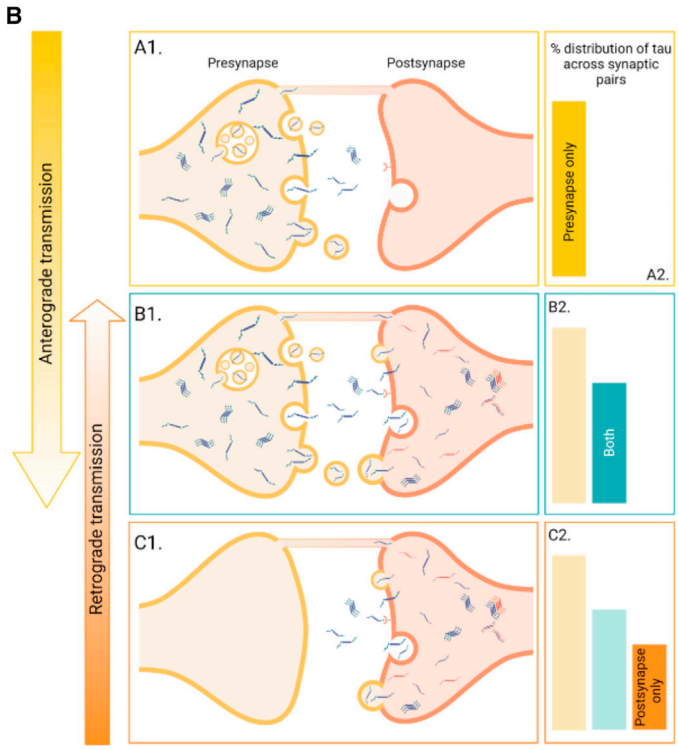

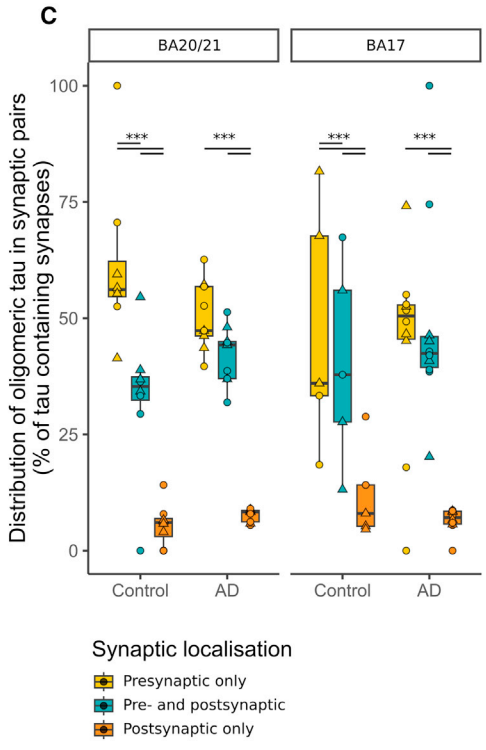

(legend on next page)

oligomeric tau.[22] Of note, both high tau seeding and high levels of tau oligomers have been linked to worse cognitive outcomes.[22,23] We also found that the proportion of oligomeric tau in presynaptic terminals was inversely correlated with the total burden of oligomeric tau. Paralleling Braak staging, these findings may imply that, i.e., while primary visual cortex does not have enough pathology to be classified as Braak stage VI, we already find oligomeric tau at synapses that may be affecting neuronal circuits.

Synaptic localization of tau may be also important for propagation of tau through the AD brain. Oligomeric tau was distributed asymmetrically across synaptic pairs. This possibly suggests a model where tau accumulates presynaptically, before release and uptake at the postsynapse, leading to tau localization in both compartments. It is unlikely that transference of pathological tau to the postsynapse from the presynaptic terminal is the only propagation mechanism. Synaptic pairs in which tau is localized to the postsynapse only could arise from retrograde transport to the postsynapse (i.e., along dendrites and spines).[64] Further, tau could undergo retrograde transport across the synapse to the presynaptic site.[65,66] However, considering the stepwise decrease in oligomeric tau localization observed at synaptic pairs (presynapse only > both terminals > postsynapse only), it is likely that tau predominantly traverses synapses in the anterograde direction. Oligomeric tau followed this pattern of distribution across synaptic pairs in both control and AD brain. However, the proportion of synapses with tau was significantly increased in AD brain, indicating that although the mode of spread may be the same, propagation likely occurs at greater frequency in AD. While these findings gave us insights into the pathogenesis of AD and can have implications in therapeutical approaches, we need to be cautious because of the inherent descriptive cross-sectional nature of postmortem studies.

Conclusions

In the present work we found that oligomeric, misfolded, and phosphorylated tau species are found at synaptic terminals of AD brains even when NFT burden is low. Given the potential early nature of these events in AD pathogenesis, we believe that these findings support the notion of multiple target- and synaptic-based approaches for therapeutic interventions.

STAR★METHODS

Detailed methods are provided in the online version of this paper and include the following:

- KEY RESOURCES TABLE
- RESOURCE AVAILABILITY
  - Lead contact
  - Materials availability
  - Data and code availability
- EXPERIMENTAL MODEL AND SUBJECT DETAILS
  - Human brain tissue
  - Mouse brain tissue
- METHOD DETAILS
  - Array tomography
  - Immunogold-electron microscopy
  - Direct STORM acquisition and image reconstruction
  - DNA-PAINT
  - DNA-PAINT analysis
  - Immunohistochemistry
  - Synaptoneurosome isolation and western blot analysis
  - Study design
- QUANTIFICATION AND STATISTICAL ANALYSIS

SUPPLEMENTAL INFORMATION

Supplemental information can be found online at https://doi.org/10.1016/j.neuron.2023.04.020.

ACKNOWLEDGMENTS

We gratefully acknowledge the contributions of our brain tissue donors and their families, the Edinburgh Brain and Tissue Bank and Alzheimer's Scotland Dementia Research Centre for coordinating brain tissue donations, Edinburgh Neuroscience for facilitating collaborations, and Prof. Rakez Kayed for generously providing T22 antibody. This work was supported by the Medical Research Council Centres of Excellence in Neurodegeneration (CoEN5025), Centro de Investigación Biomédica en Red en Enfermedades Neurodegenerativas (CIBERNED), the European Research Council (ERC) under the European Union's Horizon 2020 research and innovation program (grant agreement no. 681181), and the UK Dementia Research Institute, which receives its funding from DRI Ltd, funded by the UK Medical Research Council, Alzheimer's Society, and Alzheimer's Research UK. The confocal microscope was generously funded by Alzheimer's Research UK and a Wellcome Trust Institutional Strategic Support Fund at the University of Edinburgh. J.L. was funded by UCB Biopharma, as was the Oxford Nanoimager. M.H. and J.L. acknowledge funding from Dr. Jim Love.

AUTHOR CONTRIBUTIONS

Conceptualization, M.C.-C., C.D., M.H.H., A.L., and T.L.S.-J.; methodology, M.C.-C., M.H.H., and T.L.S.-J.; software, M.C.-C., K.H., Y.Y.C., R.I.M., L.W., and T.L.S.-J.; investigation, M.C.-C., C.D., S.S., J.-E.L., E.M.S., M.T., M.Q.-V., E.S.-A., Y.Y.C., R.I.M., J.R., J.T., T.A., O.B., and S.P.; resources, C.S.; writing – first draft, M.C.-C., C.D., M.H.H., A.L., and T.L.S.-J.; writing – editing paper, all authors; funding acquisition, A.L. and T.L.S.-J.

DECLARATION OF INTERESTS

T.S.-J. is on the Scientific Advisory Board of Cognition Therapeutics and has received honoraria for talks for industry collaborators. They did not have any

Figure 5. Insights into transsynaptic tau transmission

(A) Raw images from array tomography show the presence of pre- (magenta) and post- (cyan) synaptic terminals with oligomeric tau (yellow). The first column shows a maximum-intensity projection of raw images with a white box outlining the inset shown at top right of every image. Three consecutive 70-nm-thick sections are shown for the inset, and the synapse pointed by the arrowhead is shown below and at the last column in a 3D reconstruction.

(B) Diagram of the possible conditions found in tau synaptic distribution.

(C) Distribution of tau from pre- to postsynaptic terminals by diagnosis and brain region. Boxplots show quartiles and medians calculated from each image stack. Data points refer to case means (females, circles; males, triangles). Analysis was with linear mixed effects models including diagnostic group, sex, and pathology in the image. ***$p < 0.0001$ in post-hoc emmeans test after linear mixed effects model. Scale bars: 20 μm (raw image), 5 μm (first inset), 1 μm (second inset), approximately 500 nm (3D). See also Figure S5.

involvement in or influence over the current paper. T.S.-J. is also a member of the *Neuron* Editorial Advisory Board.

INCLUSION AND DIVERSITY

We worked to ensure gender balance in the recruitment of human subjects. We worked to ensure sex balance in the selection of non-human subjects. One or more of the authors of this paper self-identifies as an underrepresented ethnic minority in their field of research or within their geographical location. One or more of the authors of this paper self-identifies as a gender minority in their field of research. One or more of the authors of this paper self-identifies as a member of the LGBTQIA+ community. We avoided "helicopter science" practices by including the participating local contributors from the region where we conducted the research as authors on the paper.

Received: August 12, 2022
Revised: March 15, 2023
Accepted: April 17, 2023
Published: May 15, 2023

REFERENCES

1. DeKosky, S.T., and Scheff, S.W. (1990). Synapse loss in frontal cortex biopsies in Alzheimer's disease: correlation with cognitive severity. Ann. Neurol. *27*, 457–464. https://doi.org/10.1002/ana.410270502.
2. Terry, R.D., Masliah, E., Salmon, D.P., Butters, N., DeTeresa, R., Hill, R., Hansen, L.A., and Katzman, R. (1991). Physical basis of cognitive alterations in Alzheimer's disease: synapse loss is the major correlate of cognitive impairment. Ann. Neurol. *30*, 572–580. https://doi.org/10.1002/ana.410300410.
3. Serrano-Pozo, A., Frosch, M.P., Masliah, E., and Hyman, B.T. (2011). Neuropathological Alterations in Alzheimer Disease. Cold Spring Harb. Perspect. Med. *1*, a006189. https://doi.org/10.1101/cshperspect.a006189.
4. Arriagada, P.V., Growdon, J.H., Hedley-Whyte, E.T., and Hyman, B.T. (1992). Neurofibrillary tangles but not senile plaques parallel duration and severity of Alzheimer's disease. Neurology *42*, 631–639. https://doi.org/10.1212/wnl.42.3.631.
5. Bejanin, A., Schonhaut, D.R., La Joie, R., Kramer, J.H., Baker, S.L., Sosa, N., Ayakta, N., Cantwell, A., Janabi, M., Lauriola, M., et al. (2017). Tau pathology and neurodegeneration contribute to cognitive impairment in Alzheimer's disease. Brain *140*, 3286–3300. https://doi.org/10.1093/brain/awx243.
6. Kent, S.A., Spires-Jones, T.L., and Durrant, C.S. (2020). The physiological roles of tau and Aβ: implications for Alzheimer's disease pathology and therapeutics. Acta Neuropathol. *140*, 417–447. https://doi.org/10.1007/s00401-020-02196-w.
7. Hoover, B.R., Reed, M.N., Su, J., Penrod, R.D., Kotilinek, L.A., Grant, M.K., Pitstick, R., Carlson, G.A., Lanier, L.M., Yuan, L.L., et al. (2010). Tau Mislocalization to Dendritic Spines Mediates Synaptic Dysfunction Independently of Neurodegeneration. Neuron *68*, 1067–1081. https://doi.org/10.1016/j.neuron.2010.11.030.
8. Ittner, L.M., Ke, Y.D., Delerue, F., Bi, M., Gladbach, A., van Eersel, J., Wölfing, H., Chieng, B.C., Christie, M.J., Napier, I.A., et al. (2010). Dendritic function of tau mediates amyloid-beta toxicity in Alzheimer's disease mouse models. Cell *142*, 387–397. https://doi.org/10.1016/j.cell.2010.06.036.
9. Kopeikina, K.J., Polydoro, M., Tai, H.C., Yaeger, E., Carlson, G.A., Pitstick, R., Hyman, B.T., and Spires-Jones, T.L. (2013). Synaptic alterations in the rTg4510 mouse model of tauopathy. J. Comp. Neurol. *521*, 1334–1353. https://doi.org/10.1002/cne.23234.
10. Kopeikina, K.J., Wegmann, S., Pitstick, R., Carlson, G.A., Bacskai, B.J., Betensky, R.A., Hyman, B.T., and Spires-Jones, T.L. (2013). Tau causes synapse loss without disrupting calcium homeostasis in the rTg4510 model of tauopathy. PLoS One *8*, e80834. https://doi.org/10.1371/journal.pone.0080834.
11. Largo-Barrientos, P., Apóstolo, N., Creemers, E., Callaerts-Vegh, Z., Swerts, J., Davies, C., McInnes, J., Wierda, K., De Strooper, B., Spires-Jones, T., et al. (2021). Lowering Synaptogyrin-3 expression rescues Tau-induced memory defects and synaptic loss in the presence of microglial activation. Neuron *7*, 767–777. https://doi.org/10.1016/j.neuron.2020.12.016.
12. Pickett, E.K., Herrmann, A.G., McQueen, J., Abt, K., Dando, O., Tulloch, J., Jain, P., Dunnett, S., Sohrabi, S., Fjeldstad, M.P., et al. (2019). Amyloid Beta and Tau Cooperate to Cause Reversible Behavioral and Transcriptional Deficits in a Model of Alzheimer's Disease. Cell Rep. *29*, 3592–3604.e5. https://doi.org/10.1016/j.celrep.2019.11.044.
13. Zhou, L., McInnes, J., Wierda, K., Holt, M., Herrmann, A.G., Jackson, R.J., Wang, Y.C., Swerts, J., Beyens, J., Miskiewicz, K., et al. (2017). Tau association with synaptic vesicles causes presynaptic dysfunction. Nat. Commun. *8*, 15295. https://doi.org/10.1038/ncomms15295.
14. de Calignon, A., Spires-Jones, T.L., Pitstick, R., Carlson, G.A., and Hyman, B.T. (2009). Tangle-bearing neurons survive despite disruption of membrane integrity in a mouse model of tauopathy. J. Neuropathol. Exp. Neurol. *68*, 757–761. https://doi.org/10.1097/NEN.0b013e3181a9fc66.
15. Lasagna-Reeves, C.A., Castillo-Carranza, D.L., Sengupta, U., Clos, A.L., Jackson, G.R., and Kayed, R. (2011). Tau oligomers impair memory and induce synaptic and mitochondrial dysfunction in wild-type mice. Mol. Neurodegener. *6*, 39. https://doi.org/10.1186/1750-1326-6-39.
16. Schaler, A.W., Runyan, A.M., Clelland, C.L., Sydney, E.J., Fowler, S.L., Figueroa, H.Y., Shioda, S., Santa-Maria, I., Duff, K.E., and Myeku, N. (2021). PAC1 receptor-mediated clearance of tau in postsynaptic compartments attenuates tau pathology in mouse brain. Sci. Transl. Med. *13*, eaba7394. https://doi.org/10.1126/scitranslmed.aba7394.
17. Tai, H.C., Serrano-Pozo, A., Hashimoto, T., Frosch, M.P., Spires-Jones, T.L., and Hyman, B.T. (2012). The synaptic accumulation of hyperphosphorylated tau oligomers in Alzheimer disease is associated with dysfunction of the ubiquitin-proteasome system. Am. J. Pathol. *181*, 1426–1435. https://doi.org/10.1016/j.ajpath.2012.06.033.
18. Merino-Serrais, P., Benavides-Piccione, R., Blazquez-Llorca, L., Kastanauskaite, A., Rábano, A., Avila, J., and DeFelipe, J. (2013). The influence of phospho-tau on dendritic spines of cortical pyramidal neurons in patients with Alzheimer's disease. Brain *136*, 1913–1928. https://doi.org/10.1093/brain/awt088.
19. DeVos, S.L., Corjuc, B.T., Oakley, D.H., Nobuhara, C.K., Bannon, R.N., Chase, A., Commins, C., Gonzalez, J.A., Dooley, P.M., Frosch, M.P., and Hyman, B.T. (2018). Synaptic Tau Seeding Precedes Tau Pathology in Human Alzheimer's Disease Brain. Front. Neurosci. *12*, 267. https://www.frontiersin.org/articles/10.3389/fnins.2018.00267.
20. Bengoa-Vergniory, N., Velentza-Almpani, E., Silva, A.M., Scott, C., Vargas-Caballero, M., Sastre, M., Wade-Martins, R., and Alegre-Abarrategui, J. (2021). Tau-proximity ligation assay reveals extensive previously undetected pathology prior to neurofibrillary tangles in preclinical Alzheimer's disease. Acta Neuropathol. Commun. *9*, 18. https://doi.org/10.1186/s40478-020-01117-y.
21. Lasagna-Reeves, C.A., Castillo-Carranza, D.L., Sengupta, U., Sarmiento, J., Troncoso, J., Jackson, G.R., and Kayed, R. (2012). Identification of oligomers at early stages of tau aggregation in Alzheimer's disease. Faseb. J. *26*, 1946–1959. https://doi.org/10.1096/fj.11-199851.
22. Dujardin, S., Commins, C., Lathuiliere, A., Beerepoot, P., Fernandes, A.R., Kamath, T.V., De Los Santos, M.B., Klickstein, N., Corjuc, D.L., Corjuc, B.T., et al. (2020). Tau molecular diversity contributes to clinical heterogeneity in Alzheimer's disease. Nat. Med. *26*, 1256–1263. https://doi.org/10.1038/s41591-020-0938-9.
23. Singh, A., Allen, D., Fracassi, A., Tumurbaatar, B., Natarajan, C., Scaduto, P., Woltjer, R., Kayed, R., Limon, A., Krishnan, B., and Taglialatela, G. (2020). Functional Integrity of Synapses in the Central Nervous System of Cognitively Intact Individuals with High Alzheimer's Disease Neuropathology Is Associated with Absence of Synaptic Tau Oligomers. J. Alzheimers Dis. *78*, 1661–1678. https://doi.org/10.3233/JAD-200716.

24. Braak, H., and Braak, E. (1991). Neuropathological stageing of Alzheimer-related changes. Acta Neuropathol. *82*, 239–259. https://doi.org/10.1007/BF00308809.

25. Hoenig, M.C., Bischof, G.N., Seemiller, J., Hammes, J., Kukolja, J., Onur, Ö.A., Jessen, F., Fliessbach, K., Neumaier, B., Fink, G.R., et al. (2018). Networks of tau distribution in Alzheimer's disease. Brain *141*, 568–581. https://doi.org/10.1093/brain/awx353.

26. Franzmeier, N., Neitzel, J., Rubinski, A., Smith, R., Strandberg, O., Ossenkoppele, R., Hansson, O., and Ewers, M.; Alzheimer's Disease Neuroimaging Initiative ADNI (2020). Functional brain architecture is associated with the rate of tau accumulation in Alzheimer's disease. Nat. Commun. *11*, 347. https://doi.org/10.1038/s41467-019-14159-1.

27. Pooler, A.M., Phillips, E.C., Lau, D.H.W., Noble, W., and Hanger, D.P. (2013). Physiological release of endogenous tau is stimulated by neuronal activity. EMBO Rep. *14*, 389–394. https://doi.org/10.1038/embor.2013.15.

28. Frost, B., Ollesch, J., Wille, H., and Diamond, M.I. (2009). Conformational Diversity of Wild-type Tau Fibrils Specified by Templated Conformation Change. J. Biol. Chem. *284*, 3546–3551. https://doi.org/10.1074/jbc.M805627200.

29. Kaufman, S.K., Sanders, D.W., Thomas, T.L., Ruchinskas, A.J., Vaquer-Alicea, J., Sharma, A.M., Miller, T.M., and Diamond, M.I. (2016). Tau Prion Strains Dictate Patterns of Cell Pathology, Progression Rate, and Regional Vulnerability In Vivo. Neuron *92*, 796–812. https://doi.org/10.1016/j.neuron.2016.09.055.

30. Meisl, G., Hidari, E., Allinson, K., Rittman, T., DeVos, S.L., Sanchez, J.S., Xu, C.K., Duff, K.E., Johnson, K.A., Rowe, J.B., et al. (2021). In vivo rate-determining steps of tau seed accumulation in Alzheimer's disease. Sci. Adv. *7*, eabh1448. https://doi.org/10.1126/sciadv.abh1448.

31. de Calignon, A., Polydoro, M., Suárez-Calvet, M., William, C., Adamowicz, D.H., Kopeikina, K.J., Pitstick, R., Sahara, N., Ashe, K.H., Carlson, G.A., et al. (2012). Propagation of tau pathology in a model of early Alzheimer's disease. Neuron *73*, 685–697. https://doi.org/10.1016/j.neuron.2011.11.033.

32. Harris, J.A., Koyama, A., Maeda, S., Ho, K., Devidze, N., Dubal, D.B., Yu, G.Q., Masliah, E., and Mucke, L. (2012). Human P301L-mutant tau expression in mouse entorhinal-hippocampal network causes tau aggregation and presynaptic pathology but no cognitive deficits. PLoS One *7*, e45881. https://doi.org/10.1371/journal.pone.0045881.

33. Liu, L., Drouet, V., Wu, J.W., Witter, M.P., Small, S.A., Clelland, C., and Duff, K. (2012). Trans-synaptic spread of tau pathology in vivo. PLoS One *7*, e31302. https://doi.org/10.1371/journal.pone.0031302.

34. Pickett, E.K., Henstridge, C.M., Allison, E., Pitstick, R., Pooler, A., Wegmann, S., Carlson, G., Hyman, B.T., and Spires-Jones, T.L. (2017). Spread of tau down neural circuits precedes synapse and neuronal loss in the rTgTauEC mouse model of early Alzheimer's disease. Synapse *71*, e21965. https://doi.org/10.1002/syn.21965.

35. Wegmann, S., Bennett, R.E., Delorme, L., Robbins, A.B., Hu, M., McKenzie, D., Kirk, M.J., Schiantarelli, J., Tunio, N., Amaral, A.C., et al. (2019). Experimental evidence for the age dependence of tau protein spread in the brain. Sci. Adv. *5*, eaaw6404. https://doi.org/10.1126/sciadv.aaw6404.

36. Jackson, R.J., Rose, J., Tulloch, J., Henstridge, C., Smith, C., and Spires-Jones, T.L. (2019). Clusterin accumulates in synapses in Alzheimer's disease and is increased in apolipoprotein E4 carriers. Brain Commun. *1*, fcz003. https://doi.org/10.1093/braincomms/fcz003.

37. Koffie, R.M., Hashimoto, T., Tai, H.C., Kay, K.R., Serrano-Pozo, A., Joyner, D., Hou, S., Kopeikina, K.J., Frosch, M.P., Lee, V.M., et al. (2012). Apolipoprotein E4 effects in Alzheimer's disease are mediated by synaptotoxic oligomeric amyloid-β. Brain *135*, 2155–2168. https://doi.org/10.1093/brain/aws127.

38. Colom-Cadena M, Tulloch J, Jackson RJ, Catterson J.H., Rose J., Davies C., Hooley M., Anton-Fernandez A., Dunnett S., Tempelaar R., et al., . TMEM97 increases in synapses and is a potential synaptic Aβ binding partner in human Alzheimer's disease.Preprint at bioRxiv. Published online February 1, 2021:2021.02.01.428238. doi:10.1101/2021.02.01.428238

39. Aragão Gomes, L., Uytterhoeven, V., Lopez-Sanmartin, D., Tomé, S.O., Tousseyn, T., Vandenberghe, R., Vandenbulcke, M., von Arnim, C.A.F., Verstreken, P., and Thal, D.R. (2021). Maturation of neuronal AD-tau pathology involves site-specific phosphorylation of cytoplasmic and synaptic tau preceding conformational change and fibril formation. Acta Neuropathol. *141*, 173–192. https://doi.org/10.1007/s00401-020-02251-6.

40. DeKosky, S.T., and Scheff, S.W. (1990). Synapse loss in frontal cortex biopsies in Alzheimer's disease: correlation with cognitive severity. Ann. Neurol. *27*, 457–464. https://doi.org/10.1002/ana.410270502.

41. de Wilde, M.C., Overk, C.R., Sijben, J.W., and Masliah, E. (2016). Meta-analysis of synaptic pathology in Alzheimer's disease reveals selective molecular vesicular machinery vulnerability. Alzheimers Dement. *12*, 633–644. https://doi.org/10.1016/j.jalz.2015.12.005.

42. Kay, K.R., Smith, C., Wright, A.K., Serrano-Pozo, A., Pooler, A.M., Koffie, R., Bastin, M.E., Bak, T.H., Abrahams, S., Kopeikina, K.J., et al. (2013). Studying synapses in human brain with array tomography and electron microscopy. Nat. Protoc. *8*, 1366–1380. https://doi.org/10.1038/nprot.2013.078.

43. Micheva, K.D., and Smith, S.J. (2007). Array tomography: a new tool for imaging the molecular architecture and ultrastructure of neural circuits. Neuron *55*, 25–36. https://doi.org/10.1016/j.neuron.2007.06.014.

44. Scheff, S.W., DeKosky, S.T., and Price, D.A. (1990). Quantitative assessment of cortical synaptic density in Alzheimer's disease. Neurobiol. Aging *11*, 29–37. https://doi.org/10.1016/0197-4580(90)90059-9.

45. Fein, J.A., Sokolow, S., Miller, C.A., Vinters, H.V., Yang, F., Cole, G.M., and Gylys, K.H. (2008). Co-Localization of Amyloid Beta and Tau Pathology in Alzheimer's Disease Synaptosomes. Am. J. Pathol. *172*, 1683–1692. https://doi.org/10.2353/ajpath.2008.070829.

46. Henkins, K.M., Sokolow, S., Miller, C.A., Vinters, H.V., Poon, W.W., Cornwell, L.B., Saing, T., and Gylys, K.H. (2012). Extensive p-Tau Pathology and SDS-Stable p-Tau Oligomers in Alzheimer's Cortical Synapses. Brain Pathol. *22*, 826–833. https://doi.org/10.1111/j.1750-3639.2012.00598.x.

47. Sokolow, S., Henkins, K.M., Bilousova, T., Gonzalez, B., Vinters, H.V., Miller, C.A., Cornwell, L., Poon, W.W., and Gylys, K.H. (2015). Pre-synaptic C-terminal truncated tau is released from cortical synapses in Alzheimer's disease. J. Neurochem. *133*, 368–379. https://doi.org/10.1111/jnc.12991.

48. Tai, H.C., Serrano-Pozo, A., Hashimoto, T., Frosch, M.P., Spires-Jones, T.L., and Hyman, B.T. (2012). The synaptic accumulation of hyperphosphorylated tau oligomers in Alzheimer disease is associated with dysfunction of the ubiquitin-proteasome system. Am. J. Pathol. *181*, 1426–1435. https://doi.org/10.1016/j.ajpath.2012.06.033.

49. Tai, H.C., Wang, B.Y., Serrano-Pozo, A., Frosch, M.P., Spires-Jones, T.L., and Hyman, B.T. (2014). Frequent and symmetric deposition of misfolded tau oligomers within presynaptic and postsynaptic terminals in Alzheimer's disease. Acta Neuropathol. Commun. *2*, 146. https://doi.org/10.1186/s40478-014-0146-2.

50. Perez-Nievas, B.G., Stein, T.D., Tai, H.C., Dols-Icardo, O., Scotton, T.C., Barroeta-Espar, I., Fernandez-Carballo, L., de Munain, E.L., Perez, J., Marquie, M., et al. (2013). Dissecting phenotypic traits linked to human resilience to Alzheimer's pathology. Brain *136*, 2510–2526. https://doi.org/10.1093/brain/awt171.

51. Ruan, Z., Pathak, D., Venkatesan Kalavai, S., Yoshii-Kitahara, A., Muraoka, S., Bhatt, N., Takamatsu-Yukawa, K., Hu, J., Wang, Y., Hersh, S., et al. (2021). Alzheimer's disease brain-derived extracellular vesicles spread tau pathology in interneurons. Brain *144*, 288–309. https://doi.org/10.1093/brain/awaa376.

52. Spires-Jones, T.L., and Hyman, B.T. (2014). The intersection of amyloid beta and tau at synapses in Alzheimer's disease. Neuron *82*, 756–771. https://doi.org/10.1016/j.neuron.2014.05.004.

53. Kopeikina, K.J., Polydoro, M., Tai, H.C., Yaeger, E., Carlson, G.A., Pitstick, R., Hyman, B.T., and Spires-Jones, T.L. (2013). Synaptic alterations in the

rTg4510 mouse model of tauopathy. J. Comp. Neurol. *521*, 1334–1353. https://doi.org/10.1002/cne.23234.

54. Kopeikina, K.J., Wegmann, S., Pitstick, R., Carlson, G.A., Bacskai, B.J., Betensky, R.A., Hyman, B.T., and Spires-Jones, T.L. (2013). Tau causes synapse loss without disrupting calcium homeostasis in the rTg4510 model of tauopathy. PLoS One *8*, e80834. https://doi.org/10.1371/journal.pone.0080834.
55. Polydoro, M., Acker, C.M., Duff, K., Castillo, P.E., and Davies, P. (2009). Age-Dependent Impairment of Cognitive and Synaptic Function in the htau Mouse Model of Tau Pathology. J. Neurosci. *29*, 10741–10749. https://doi.org/10.1523/JNEUROSCI.1065-09.2009.
56. Fá, M., Puzzo, D., Piacentini, R., Staniszewski, A., Zhang, H., Baltrons, M.A., Li Puma, D.D., Chatterjee, I., Li, J., Saeed, F., et al. (2016). Extracellular Tau Oligomers Produce An Immediate Impairment of LTP and Memory. Sci. Rep. *6*, 19393. https://doi.org/10.1038/srep19393.
57. Hill, E., Karikari, T.K., Moffat, K.G., Richardson, M.J.E., and Wall, M.J. (2019). Introduction of Tau Oligomers into Cortical Neurons Alters Action Potential Dynamics and Disrupts Synaptic Transmission and Plasticity. eNeuro *6*. ENEURO.0166-19.2019. https://doi.org/10.1523/ENEURO.0166-19.2019.
58. Ondrejcak, T., Klyubin, I., Corbett, G.T., Fraser, G., Hong, W., Mably, A.J., Gardener, M., Hammersley, J., Perkinton, M.S., Billinton, A., et al. (2018). Cellular Prion Protein Mediates the Disruption of Hippocampal Synaptic Plasticity by Soluble Tau In Vivo. J. Neurosci. *38*, 10595–10606. https://doi.org/10.1523/JNEUROSCI.1700-18.2018.
59. Puzzo, D., Piacentini, R., Fá, M., Gulisano, W., Li Puma, D.D., Staniszewski, A., Zhang, H., Tropea, M.R., Cocco, S., Palmeri, A., et al. (2017). LTP and memory impairment caused by extracellular Aβ and Tau oligomers is APP-dependent. Elife *6*, e26991. https://doi.org/10.7554/eLife.26991.
60. Castillo-Carranza, D.L., Gerson, J.E., Sengupta, U., Guerrero-Muñoz, M.J., Lasagna-Reeves, C.A., and Kayed, R. (2014). Specific Targeting of Tau Oligomers in Htau Mice Prevents Cognitive Impairment and Tau Toxicity Following Injection with Brain-Derived Tau Oligomeric Seeds. J. Alzheimers Dis. *40*, S97–S111. https://doi.org/10.3233/JAD-132477.
61. Kaniyappan, S., Chandupatla, R.R., Mandelkow, E.M., and Mandelkow, E. (2017). Extracellular low-n oligomers of tau cause selective synaptotoxicity without affecting cell viability. Alzheimers Dement. *13*, 1270–1291. https://doi.org/10.1016/j.jalz.2017.04.002.
62. Usenovic, M., Niroomand, S., Drolet, R.E., Yao, L., Gaspar, R.C., Hatcher, N.G., Schachter, J., Renger, J.J., and Parmentier-Batteur, S. (2015). Internalized Tau Oligomers Cause Neurodegeneration by Inducing Accumulation of Pathogenic Tau in Human Neurons Derived from Induced Pluripotent Stem Cells. J. Neurosci. *35*, 14234–14250. https://doi.org/10.1523/JNEUROSCI.1523-15.2015.
63. DeVos, S.L., Corjuc, B.T., Oakley, D.H., Nobuhara, C.K., Bannon, R.N., Chase, A., Commins, C., Gonzalez, J.A., Dooley, P.M., Frosch, M.P., and Hyman, B.T. (2018). Synaptic Tau Seeding Precedes Tau Pathology in Human Alzheimer's Disease Brain. Front. Neurosci. *12*, 267. https://www.frontiersin.org/article/10.3389/fnins.2018.00267.
64. Hoover, B.R., Reed, M.N., Su, J., Penrod, R.D., Kotilinek, L.A., Grant, M.K., Pitstick, R., Carlson, G.A., Lanier, L.M., Yuan, L.L., et al. (2010). Tau Mislocalization to Dendritic Spines Mediates Synaptic Dysfunction Independently of Neurodegeneration. Neuron *68*, 1067–1081. https://doi.org/10.1016/j.neuron.2010.11.030.
65. Ahmed, Z., Cooper, J., Murray, T.K., Garn, K., McNaughton, E., Clarke, H., Parhizkar, S., Ward, M.A., Cavallini, A., Jackson, S., et al. (2014). A novel in vivo model of tau propagation with rapid and progressive neurofibrillary tangle pathology: the pattern of spread is determined by connectivity, not proximity. Acta Neuropathol. *127*, 667–683. https://doi.org/10.1007/s00401-014-1254-6.
66. Wu, J.W., Herman, M., Liu, L., Simoes, S., Acker, C.M., Figueroa, H., Steinberg, J.I., Margittai, M., Kayed, R., Zurzolo, C., et al. (2013). Small Misfolded Tau Species Are Internalized via Bulk Endocytosis and Anterogradely and Retrogradely Transported in Neurons. J. Biol. Chem. *288*, 1856–1870. https://doi.org/10.1074/jbc.M112.394528.
67. Hesse, R., Hurtado, M.L., Jackson, R.J., Eaton, S.L., Herrmann, A.G., Colom-Cadena, M., Tzioras, M., King, D., Rose, J., Tulloch, J., et al. (2019). Comparative profiling of the synaptic proteome from Alzheimer's disease patients with focus on the APOE genotype. Acta Neuropathol. Commun. *7*, 214. https://doi.org/10.1186/s40478-019-0847-7.
68. Kumle, L., Võ, M.L.H., and Draschkow, D. (2021). Estimating power in (generalized) linear mixed models: An open introduction and tutorial in R. Behav Res *53*, 2528–2543. https://doi.org/10.3758/s13428-021-01546-0.
69. Pooler, A.M., Polydoro, M., Wegmann, S.K., Pitstick, R., Kay, K.R., Sanchez, L., Carlson, G.A., Gomez-Isla, T., Albers, M.W., Spires-Jones, T.L., and Hyman, B.T. (2013). Tau-amyloid interactions in the rTgTauEC model of early Alzheimer's disease suggest amyloid-induced disruption of axonal projections and exacerbated axonal pathology. J. Comp. Neurol. *521*, 4236–4248. https://doi.org/10.1002/cne.23411.
70. Santacruz, K., Lewis, J., Spires, T., Paulson, J., Kotilinek, L., Ingelsson, M., Guimaraes, A., DeTure, M., Ramsden, M., McGowan, E., et al. (2005). Tau suppression in a neurodegenerative mouse model improves memory function. Science *309*, 476–481. https://doi.org/10.1126/science.1113694.
71. Spires, T.L., Orne, J.D., SantaCruz, K., Pitstick, R., Carlson, G.A., Ashe, K.H., and Hyman, B.T. (2006). Region-specific dissociation of neuronal loss and neurofibrillary pathology in a mouse model of tauopathy. Am. J. Pathol. *168*, 1598–1607. https://doi.org/10.2353/ajpath.2006.050840.
72. Yetman, M.J., Lillehaug, S., Bjaalie, J.G., Leergaard, T.B., and Jankowsky, J.L. (2016). Transgene expression in the Nop-tTA driver line is not inherently restricted to the entorhinal cortex. Brain Struct. Funct. *221*, 2231–2249. https://doi.org/10.1007/s00429-015-1040-9.
73. Alafuzoff, I., Pikkarainen, M., Al-Sarraj, S., Arzberger, T., Bell, J., Bodi, I., Bogdanovic, N., Budka, H., Bugiani, O., Ferrer, I., et al. (2006). Interlaboratory comparison of assessments of Alzheimer disease-related lesions: a study of the BrainNet Europe Consortium. J. Neuropathol. Exp. Neurol. *65*, 740–757. https://doi.org/10.1097/01.jnen.0000229986.17548.27.
74. Braak, H., Alafuzoff, I., Arzberger, T., Kretzschmar, H., and Del Tredici, K. (2006). Staging of Alzheimer disease-associated neurofibrillary pathology using paraffin sections and immunocytochemistry. Acta Neuropathol. *112*, 389–404. https://doi.org/10.1007/s00401-006-0127-z.
75. Colom-Cadena, M., Gelpi, E., Charif, S., Belbin, O., Blesa, R., Martí, M.J., Clarimón, J., and Lleó, A. (2013). Confluence of α-synuclein, tau, and β-amyloid pathologies in dementia with Lewy bodies. J. Neuropathol. Exp. Neurol. *72*, 1203–1212. https://doi.org/10.1097/NEN.0000000000000018.
76. Colom-Cadena, M., Pegueroles, J., Herrmann, A.G., Henstridge, C.M., Muñoz, L., Querol-Vilaseca, M., Martín-Paniello, C.S., Luque-Cabecerans, J., Clarimon, J., Belbin, O., et al. (2017). Synaptic phosphorylated α-synuclein in dementia with Lewy bodies. Brain *140*, 3204–3214. https://doi.org/10.1093/brain/awx275.
77. Olivier, N., Keller, D., Gönczy, P., and Manley, S. (2013). Resolution Doubling in 3D-STORM Imaging through Improved Buffers. PLoS One *8*, e69004. https://doi.org/10.1371/journal.pone.0069004.
78. van der Zwaag, D., Vanparijs, N., Wijnands, S., De Rycke, R., De Geest, B.G., and Albertazzi, L. (2016). Super Resolution Imaging of Nanoparticles Cellular Uptake and Trafficking. ACS Appl. Mater. Interfaces *8*, 6391–6399. https://doi.org/10.1021/acsami.6b00811.
79. Bankhead, P., Loughrey, M.B., Fernández, J.A., Dombrowski, Y., McArt, D.G., Dunne, P.D., McQuaid, S., Gray, R.T., Murray, L.J., Coleman, H.G., et al. (2017). QuPath: Open source software for digital pathology image analysis. Sci. Rep. *7*, 16878. https://doi.org/10.1038/s41598-017-17204-5.
80. R Core Team (2021). R: A language and environment for statistical computing. https://www.r-project.org/.

STAR★METHODS

KEY RESOURCES TABLE

REAGENT or RESOURCE	SOURCE	IDENTIFIER
Antibodies		
Rabbit anti-PSD95 (D27E11)	Cell Signaling Technology	Cat#3450; RRID:AB_2292883
Mouse anti-PSD95 (K28/43)	DSHB	Cat#K28/43; RRID:AB_2877189
Mouse anti-PSD95 (K28/43)	Neuromab	Cat#MABN68
Guinea pig anti-PSD95	Synaptic Systems	Cat#124 014; RRID:AB_2619800
Mouse anti-synaptophysin (SY38)	Abcam	Cat#ab8049; RRID:AB_2198854
Recombinant Alexa Fluor® 488 Anti-Synaptophysin antibody [YE269]	Abcam	Cat#ab196379; RRID:AB_2922671
Goat anti-synaptophysin	R&D Systems	Cat#AF5555; RRID:AB_2198864
Mouse anti-conformational tau (Alz50)	Courtesy of P. Davies Albert Einstein College of Medicine; New York; USA	Cat#Alz50; RRID:AB_2313937
Mouse anti-phosphorylated tau (AT8)	Thermo Fisher	Cat#MN1020; RRID:AB_223647
Mouse anti-phosphorylated tau (AT8)	Innogenetics	Cat#90206
Rabbit anti-oligomeric tau (T22, serum)	Courtesy of Rakez Kayed	NA
Rabbit anti-oligomeric tau (T22, purified)	Millipore	Cat#ABN454-I; RRID:AB_2888681
Mouse anti-Tau (Tau5)	BioLegend	Cat#806401; RRID:AB_2564705
Rabbit anti-GADPH	Cell Signaling	Cat#2118; RRID:AB_561053
Mouse anti-B-actin	Cell Signaling	Cat#3700; RRID:AB_2242334
Rabbit anti-VAMP2 (D6O1A)	Cell Signaling	Cat#13508; RRID:AB_2798240
Chicken anti-GFP	Ayes Labs	Cat#GFP-1020; RRID:AB_10000240
Donkey anti-rabbit Alexa Fluor 488®	Invitrogen	Cat#A-21206; RRID:AB_2535792
Donkey anti-rabbit Alexa Fluor 488®	Thermo Fisher	Cat#A-21206; RRID:AB_2535792
Donkey anti-mouse Alexa Fluor 488®	Thermo Fisher	Cat#A-21202; RRID:AB_141607
Donkey anti-guinea pig Alexa Fluor 488®	Jackson ImmunoResearch	Cat#706-545-148; RRID:AB_2340472
Goat anti-Chicken Alexa Fluor 488®	Thermo Fisher	Cat#A-11039; RRID:AB_142924
Goat anti-mouse Alexa Fluor 594®	Invitrogen	Cat#A-21044; RRID:AB_141424
Goat anti-Guinea Pig Alexa Fluor 594®	Thermo Fisher	Cat#A-11076; RRID:AB_141930
Donkey anti-Mouse Cy3-AffiniPure	Jackson ImmunoResearch Labs	Cat#715-165-150; RRID:AB_2340813
Goat anti-mouse Alexa Fluor 647®	Invitrogen	Cat#A-21240; RRID:AB_141658
Donkey anti-rabbit Alexa Fluor 647®	Thermo Fisher	Cat#A-21447; RRID:AB_141844
Goat anti-rabbit Alexa Fluor 647®	Thermo Fisher	Cat#A-21244; RRID:AB_2535812
Donkey anti-Rabbit Cy5-AffiniPure	Jackson ImmunoResearch Labs	Cat#711-175-152; RRID:AB_2340607
Goat anti-mouse DyLight™ 405	BioLegend	Cat#409109; RRID:AB_10642830
Goat anti-Rabbit IR Dye 800	Li-COR BioSciences	Cat#926–32211; RRID:AB_621843
Goat anti-Mouse IR Dye 700	Li-COR BioSciences	Cat#926–32220; RRID:AB_621840
Goat anti-Rabbit IgG - H&L - F(ab)2 Fragment Polyclonal Antibody, 10nm Gold Conjugated	Abcam	Cat#ab39601; RRID:AB_954434
Donkey anti-Rabbit IgG (H + L) Cross-Adsorbed Secondary Antibody	Thermo Fisher	Cat#31238; RRID:AB_429690
Biological samples		
Post-mortem human brain samples	Edinburgh Brain Bank	NA
Chemicals, peptides, and recombinant proteins		
LR white resin medium	Electron Microscopy Sciences	Cat#14381
DAPI	Sigma Aldrich	Cat#D9542
Osmium tetroxide	TAAB Laboratories	Cat#O014

(*Continued on next page*)

Please cite this article in press as: Colom-Cadena et al., Synaptic oligomeric tau in Alzheimer's disease — A potential culprit in the spread of tau pathology through the brain, Neuron (2023), https://doi.org/10.1016/j.neuron.2023.04.020

Continued

REAGENT or RESOURCE	SOURCE	IDENTIFIER
Propylene oxide	Agar Scientific	Cat#AGR1080
Formvar-coated nickel grids	Agar Scientific	Cat#S162N1
ATTO655-tagged imager strand	ATDBio Ltd	GGTGGT-ATTO655
Cy3B-tagged imager strand	ATDBio Ltd	AGAGAGAX-Cy3B
100 kDa Amicon column	Merk	Cat#UFC510024
Critical commercial assays		
Novolink Polymer Detection Systems	Leica Biosystems	Cat#RE7200-CE
Siteclick Antibody Azido modification Kit	Thermo Fisher Scientific	Cat#S20026
Experimental models: Organisms/strains		
FVB-*Fgf14*$^{Tg(tetO\text{-}MAPT^{*}P301L)4510Kha}$/JlwsJ	The Jackson Laboratory	Cat#015815; RRID:IMSR_JAX:015815
Tg(tetO-tdTomato,-Syp/EGFP*)1.1Luo/J	The Jackson Laboratory	Cat#012345; RRID:IMSR_JAX:01234
Oligonucleotides		
5xR2 (Docking2): 5′-2ACCACCACCACCACCACCA-3′	ATDBio	NA
7xR3 (Docking3): 5′-2CTCTCTCTCTCTCTCTCTC-3′	ATDBio	NA
R2_6nt (Imaging2): 5′-GGTGGT-ATTO655-3′	ATDBio	NA
R3_6nt (Imaging3): 5′-AGAGAGAX-Cy3B-3′	ATDBio	NA
Software and algorithms		
MATLAB	MathWorks (https://www.mathworks.com)	RRID:SCR_001622
ImageJ	National Institutes of Health (https://imagej.nih.gov/ij/)	RRID:SCR_003070
R	R Project for Statistical Computing (http://www.r-project.org/)	RRID:SCR_001905
Inkscape	Inkscape (https://inkscape.org/)	RRID:SCR_014479
Imaris	Imaris (http://www.bitplane.com/imaris/imaris)	RRID:SCR_007370
Python	Python Programming Language (https://www.python.org/)	RRID:SCR_008394
Zeiss ZEN	ZEN Digital Imaging for Light Microscopy (https://www.zeiss.com/microscopy/en/products/software/zeiss-zen.html)	RRID:SCR_013672
Leica Application Suite X	Leica Application Suite X (https://www.leica-microsystems.com/products/microscope-software/details/product/leica-las-x-ls/)	RRID:SCR_013673
NimOS Software	Oxford Nanoimager software (ONI, https://oni.bio/nanoimager/software/nimos-software/)	NA
Nikon NIS element	NIS-Elements (https://www.nikoninstruments.com/Products/Software)	RRID:SCR_014329
QuPath	QuPath (https://qupath.github.io/)	RRID:SCR_018257
Custom MATLAB, R, ImageJ scripts	This paper	https://github.com/Spires-Jones-Lab

RESOURCE AVAILABILITY

Lead contact

Further information and requests for resources and reagents should be directed to and will be fulfilled by the lead contact, Prof. Tara Spires-Jones (tara.spires-jones@ed.ac.uk).

Materials availability

This study did not generate new unique reagents.

Data and code availability

- Spreadsheets of analyzed data and statistical analysis codes are available in the University of Edinburgh DataShare repository at https://doi.org/10.7488/ds/3837.
- Raw images are available from the University of Edinburgh DataVault with the link provided upon reasonable request. Original western blot images are included in the supplementary data.
- Image analysis scripts are freely available on GitHub (https://github.com/Spires-Jones-Lab).
- Any additional information required to reanalyze the data reported in this paper is available from the lead contact upon request.

EXPERIMENTAL MODEL AND SUBJECT DETAILS

Human brain tissue

Brain samples were obtained with ethical approval via the University of Edinburgh Sudden Death Brain Bank and the Alzheimer Scotland Brain and Tissue Bank. This study was reviewed and approved by the Edinburgh Brain Bank ethics committee and the Academic and Clinical Central Office for Research and Development, a joint office of the University of Edinburgh and NHS Lothian (approval number 15-HV-016). The Edinburgh Brain Bank is a Medical Research Council funded facility with research ethics committee (REC) approval (16/ES/0084).

Inclusion criteria for Alzheimer's disease cases were a clinical dementia diagnosis, Braak stage V-VI, and neuropathological diagnosis of AD. Control subjects were donors without neurological or psychiatric diagnoses and were included based on age, sex, and *APOE* genotype matching the AD cases as closely as possible. All cases were genotyped in-house to determine *APOE* genotype, as described previously.[67] Exclusion criteria for both groups were neuropathological findings indicative of substantial secondary pathology (e.g., hemorrhage or Lewy bodies within brain region of interest). A total of 23 AD and 19 control cases were examined in this study as outlined in Table 1 showing demographic data and the experiments they were used in. Sex was included as a fixed effect in statistical models to examine sex effects in all measures.

A statistical power analysis was performed for sample size estimation, based on data from study 1 (Tables 1 and S1), comparing presynaptic terminals with tau to diagnosis (control or AD) by linear mixed effect model (effect size $\beta = 0.521$, see statistical analysis section). With an alpha = 0.05 and power = 0.80, the projected sample size needed with this effect size in approximately N = 10. The analysis was performed as described in.[68]

Brain samples from inferior temporal cortex (Broadmann Areas 20 and 21, BA20/21) and primary visual cortex (BA17) were collected at autopsy and preserved by fixation and paraffin embedding, and fixation for array tomography as detailed previously.[42] These regions were selected to compare areas with high pathological burden (BA20/21) to those with low pathology (BA17).

Mouse brain tissue

Mice expressing human P301L mutant tau, cytoplasmic tdTomato, and green fluorescent protein tagged synaptophysin in entorhinal cortex neurons were used to determine whether oligomeric tau can spread anterogradely from pre to post synapses. Tissue was used from mice generated in a previous study.[34,69] Briefly, FVB-Tg(tetO-Tau$_{P301L}$)4510 mice[70,71] were crossed with the Tg(tetO-tdTomato-Syp/mut4EGFP)1.1Luo/J line from Jackson laboratories. Offspring expressing both Tg(tetO-Tau$_{P301L}$)4510 and Tg(tetO-tdTomato-Syp/mut4EGFP) transgenes were crossed with a line expressing the tetracycline sensitive transcriptional activator controlled by the Klk8 neuropsin promotor (EC-tTA), which expresses the tTA heavily in the EC and not at all in the dentate gyrus.[72] These crosses generated mice expressing both rTgTauEC + EC-tdTomato/Syp-GFP. Blocks containing entorhinal cortex and hippocampus were sectioned for array tomography from both male and female animals at 3 months (n = 3), 9 months (n = 4) and 18 months (n = 4). A mouse without P301L Tau expression which did express tdTomato and GFP was included as a negative control for T22 staining and there was a no primary negative control condition. Animals were maintained on a 12h light/dark cycle with *ad libitum* access to food and water. All animal experiments were approved by the Harvard Medical School Institutional Animal Care and Use Committee and the UK Home Office.

METHOD DETAILS

Array tomography

Tissue samples were fixed in 4% paraformaldehyde for 3 h, dehydrated, and embedded in LR White resin. 70nm serial sections were cut with a diamond knife (Diatome) using an ultracut microtome (Leica). Ribbons of 15–30 serial sections were collected onto gelatin coated coverslips and immunostained with antibody combinations shown in Table S1. Images were obtained with a 63x 1.4 NA objective on an AxioImager (Zeiss) or Leica TCS confocal (Leica). In study 1, images were taken in regions containing NFTs, dystrophic neurites surrounding plaques, or no pathological lesions. Pathological lesions were identified by 2 experienced investigators (CD and MCC) based on international guidelines as we have used previously (Figure S1).[73–75] Only one microscope was used for imaging each experimental condition. Image from the same location in each serial section along a ribbon were aligned, thresholded, and parameters quantified using in house scripts in ImageJ, MATLAB (Mathworks), and Python. All software is freely available on GitHub (https://github.com/Spires-Jones-Lab). Saturation was minimized during image acquisition and only applied for figure visualization.

3D reconstructions were performed with Imaris software (Bitplane). For more details, please see our methods video demonstrating this technique at https://doi.org/10.7488/ds/297.

Immunogold-electron microscopy

Tissue samples were collected at autopsy and fixed in 4% paraformaldehyde and 0.1% glutaraldehyde in 0.1M phosphate buffer (PB) for 48 h at 4°C. After fixation, the tissue was washed with 0.1M PB twice and stored at 4°C prior to processing and embedding. Tissue processing was carried out using an Electron Microscope Tissue Processor (Leica). In the processor, the tissue was first placed in 0.1% osmium tetroxide (O014, TAAB Laboratories) in boiled distilled water for 1 h. Thereafter, samples were dehydrated in a series of solutions in preparation for embedding: 3 cycles of 5 min each in boiled distilled water, 50% ethanol, 70% ethanol and 90% ethanol. This is followed by 2 cycles of 15 min in 100% ethanol, and 2 cycles of 2 min in propylene oxide. The samples were then placed in a mixture of half propylene oxide (AGR1080, Agar Scientific) and half LR white resin (AGR1281, Agar Scientific) for 30 min, before being transferred to a full solution of LR white resin for 2 cycles of 30 min. These tissues were then taken out of the processor, placed in a gelatin capsule (C087/1, TAAB Laboratories), and filled up with LR white resin to the brim. Polymerization of the LR white resin was allowed to occur by thermal curing at 52°C for 24 h. These resin-embedded tissue blocks were then stored at room temperature until ready for immuno-EM staining.

The resin-embedded tissue blocks were cut into 50nm ultrathin sections using an ultramicrotome (UC6, Leica) fitted with a Histo Jumbo Diamond Knife (Diatome Knives) and placed onto formvar-coated nickel grids (S162N1, Agar Scientific). Prior to immuno-EM staining, residual osmium tetroxide in the tissue were removed by incubating the tissue-covered nickel grids in saturated sodium metaperiodate in boiled distilled water for 1 min. The nickel grids were then incubated in 1% sodium borohydride in 0.1M PB for 5 min to reduce free aldehydes, and thereafter incubated in 50mM glycine in 0.1M PB for 10 min to inactivate residual aldehyde groups. The nickel grids were then blocked in blocking buffer (0.1% BSA, 0.1% fish skin gelatin, 0.05% Tween in 0.2M PB, pH7.4) for 1 h at room temperature. Rabbit T22 primary antibody (1:50, courtesy Dr Rakez Kayed) was diluted in antibody dilution buffer (0.1% BSA, 150mM sodium chloride in 0.2M PB, pH7.4) and incubated with the nickel grids overnight at 4°C. The next day, the nickel grids were washed in 6 rinses of 0.2M PB. Goat anti-rabbit 10nm gold-conjugated secondary antibody (1:50, ab39601, Abcam) was diluted in antibody dilution buffer and incubated with the nickel grids for 90 min at room temperature. The nickel grids were then washed in 6 rinses of 0.2M PB, fixed in 2.5% glutaraldehyde in 0.2M PB for 15 min, and washed in 6 rinses of 0.2M PB again. Negative staining of the nickel grids was carried out to improve imaging contrast. This was done in a carbon dioxide free environment: incubated the nickel grids with 3% uranyl acetate in 50% ethanol for 15 min and 3% lead citrate in boiled distilled water for 150 s, rinsed thrice in boiled distilled water in between the steps. Once the nickel grids were dry, images were captured using a Transmission Electron Microscope (JEM-1400 Plus, JOEL) and viewed using ImageJ (Version 1.44).

Direct STORM acquisition and image reconstruction

For the reconstruction of the images using direct STORM, sections 70 nm thick were stained as previously described,[76] using the primary antibodies T22 (Millipore) or AT8 (Innogenetics) and Synaptophysin (R&D Systems), and the secondary antibodies Alexa 488 (ThermoFisher) and Alexa 647 (ThermoFisher), finally stained with Hoechst 33258 (Life Technologies) to visualize the nuclei, then the coverslips were mounted with OXEA buffer.[77] STORM images were acquired using a Nikon N-STORM system configured for total internal reflection fluorescence (TIRF) imaging. Laser inclination was tuned to adjust focus and to maximize the signal-to-noise ratio. Alexa Fluor 647 was excited illuminating the sample with the 647 nm (20% of 160 mW) and Alexa Fluor 488 with the 488 (40% of 80 mW) lasers line built into the microscope. Fluorescence was collected by means of a Nikon 100x, 1.49 NA oil immersion objective and passed through a quad-band pass dichroic filter (97335 Nikon). 10,000 frames at 20 ms integration time were acquired for each channel. Images were recorded onto a 256 × 256 pixel region of a Hamamatsu ORCA Flash 4.0 CMOS camera (0.16 μm pixel size). STORM images were analyzed with the STORM module of the NIS element Nikon software.[78]

DNA-PAINT

DNA Conjugation to the AT8 and T22 antibodies and donkey anti-rabbit IgG (H + L) cross-absorbed secondary antibody (Invitrogen, 31238) was performed using the Siteclick Antibody Azido modification Kit (Thermo Fisher Scientific, S20026) according to the manufacturer's instructions. Briefly, after buffer exchange, 200 μg of the AT8, T22 antibodies and secondary antibody were incubated for 6 h at 37°C with β-galactosidase. To conjugate an azido group to the antibodies, they were incubated overnight at 30°C in a mixture of UDP-GalNAz and GalT enzyme. After purification, the modified antibodies were incubated with DBCO-DNA (2-ACCACCACCAC CACCACCA, 2 = 5′ DBCO TEG, ATDBio Ltd.) in a 1:5 ratio overnight at 25°C. The remaining unconjugated DNA was removed with 100 kDa Amicon columns (Merck, UFC510024).

Frame seal slide chambers (9 × 9 mm, Biorad, Hercules, USA) were affixed to the AT sections onto the coverslip, which were stained as previously described (Kay et al.[42]) 1) using AF488-labeled synaptophysin (1/100 dilution) and either DNA-conjugated AT8 (100 nM) or DNA-conjugated T22 (100 nM) antibodies or 2) using PSD95 (Cell Signaling Technology, D27E11 XP rabbit mAb) (1/50 dilution) and DNA-conjugated donkey anti-rabbit IgG (H + L) cross-absorbed secondary antibody with either DNA-conjugated AT8 (100M) or DNA-conjugated T22 (100nM) antibodies. ATTO655-tagged imager strand (GGTGGT-ATTO655, ATDBio Ltd.) was diluted in GLOX buffer (40 μg/mL Catalase, 0.5 mg/mL glucose oxidase, 10% w/v glucose and 200 mM β-mercaptoethanol) and used at a final imaging concentration of 2nM or 4 nM. Cy3B-tagged imager strand (AGAGAGAX-Cy3B, ATDBio Ltd.) was diluted

in imaging buffer (5 mM Tris-HCl pH 8.0, 1mM EDTA, 75 mM MgCl2, 0.05% Tween 20) and at a final imaging concentration of 2 nM.

DNA-PAINT for synaptophysin and AT8 or T22 combined with dSTORM was performed on an Oxford NanoImager (ONI) super-resolution microscope equipped with four laser lines (405, 488, 561, and 638 nm) and a 100× oil-immersion objective (Olympus 1.49 NA). Fluorescence images were acquired by exciting multiple 50 μm × 80 μm areas with 488 nm laser for AF488-labeled synaptophysin (dSTORM, laser power 44–47 mW, interval excitation with 405 nm laser per 200 frames, 5,000 frames with an exposure time of 50 ms) or 638 nm laser for ATTO655-tagged imaging strands targeting the conjugated AT8 or T22 antibodies (DNA-PAINT, laser power 60–66mW, 5,000 frames with an exposure time of 50 ms). The laser was set at 53° incidence angle. Images were recorded by NimOS software associated with the ONI instrument.

DNA-PAINT for PSD95 and AT8 or T22 was performed using a custom-built TIRF microscope, restricting excitation of fluorophores within the sample to 200 nm from the sample-coverslip interface. The fluorophores were excited at either 561 nm (Cy3B) or 638 nm (ATTO655). Collimated laser light at wavelengths of 561 nm (Cobolt DPL561-100 DPSS Laser System, Cobalt, Sweden) and 638 nm (Cobolt DPL638-100 DPSS Laser System, Cobalt, Sweden) were aligned and directed parallel to the optical axis at the edge of a 1.49 NA TIRF Objective (CFI Apochromat TIRF 60XC Oil, Nikon, Japan), mounted on an inverted Nikon TI2 microscope (Nikon, Japan). A perfect-focus system corrected the imaging process for any stage-drift. Fluorescence was collected by the same objective and separated from the TIR beam by a dichroic mirror Di01-R405/488/561/635 (Semrock, Rochester, NY, USA). Collected light was then passed through appropriate filters (561 nm: LP02-568-RS, FF01-587/35 (Semrock, NY, USA, 638 nm: FF01-432/515/595/730-25, LP02-647RU-25 (Semrock, NY, USA)). The emission beam was passed through a 2.5x beam expander and focused onto an EMCCD camera for image collection (Delta Evolve 512, Photometrics, Tucson, AZ, USA) operating in frame transfer mode (EMGain = 11.5 e^{-}/ADU and 250 ADU/photon). Pixel size was 103 nm. Images were recorded with an exposure time of 50 ms with 638 nm illumination, followed by 561 nm excitation. The microscope was automated using the open-source microscopy platform Micromanager (NIH, Bethesda).

DNA-PAINT analysis

The positions of the transiently immobilized DNA imager strands within each frame were determined using the PeakFit plugin (an ImageJ/Fiji plugin of the GDSC Single Molecule Light Microscopy package (http://www.sussex.ac.uk/gdsc/intranet/microscopy/imagej/gdsc_plugins) for ImageJ using a 'signal strength' threshold of 50 and a precision threshold of 20 nm.

Immunohistochemistry

Paraffin sections were stained with AT8 using the Novolink polymer detection system and visualized using 3,3′-diaminobenzideine chromogen then counterstained with hematoxylin to stain nuclei. ROIs containing cortical gray matter were delineated using QuPath[79] and color deconvolved in ImageJ. Using a custom MATLAB script, neurofibrillary tangles were identified minimizing the bias from manual counting.

Synaptoneurosome isolation and western blot analysis

Brain homogenates (H) and synaptoneurosomes (S) were prepared as described in.[48] In brief, ~200 mg of tissue from BA20/21 was homogenized on ice in 1mL homogenization buffer (25 mM HEPES pH 7.5, 120 mM NaCl, 5 mM KCl, 1 mM MgCl2, 2 mM CaCl2, protease inhibitors (Roche complete mini), phosphatase inhibitors (Millipore, 524,629). The homogenate was filtered through an 80 μm nylon filter (Millipore, NY8002500) and 300 μL was saved as crude homogenate with buffer (100 mM/L Tris-HC1 pH 7.6, 4% SDS, protease inhibitor cocktail EDTA-free 100x Thermo Fisher Scientific, Loughborough, UK). The remaining crude homogenate was further filtered through a 5 μm filter (Millipore, SLSV025NB) and centrifuged at 1000 g for 5 min. The supernatant was discarded and the pellet was washed with buffer and centrifuged again, yielding the synaptoneurosome pellet. For storage it was mixed with buffer (100 mM/L Tris-HC1 pH 7.6, 4% SDS, protease inhibitor cocktail EDTA-free 100x Thermo Fisher Scientific, Loughborough, UK). Protein concentrations were determined using a protein assay (Micro BCA TM Protein Assay Kit, Thermo Fisher Scientific, 23235).

Synaptoneurosomes preparations (2.5–10 μg/μL) were denatured at 95°C for 5 min. To detect oligomeric tau, 75 μg of protein were resolved using 4%–12% Bis–Tris gels (MOPS running) and transferred onto nitrocellulose membranes (Biorad, 1620112) in Trans-Blot turbo buffer (Biorad, 1704270) supplemented with 20% ethanol at 25 mV for 13 min in the Trans-Blot Turbo Transfer System (Biorad, 1704150). After blocking 1h with Intercept Blocking Buffer (Li-COR; 927–60001), the membrane was incubated with the indicated primary antibodies (α-tau5 antibody (Biolegend, 806401, 1:250) and α-GAPDH antibody (Cell Signaling, 2118,1:1000) overnight at 4°C. The protein bands were visualized using corresponding fluorescent secondary antibodies (Odyssey, 1:5,000). Infrared fluorescence was measured with the Odyssey CLx imager (LI-COR) and quantified using Image Studio software (Li-COR Biosciences).

Study design

The immunostaining, image acquisition, image processing and analyses were performed blinded to the clinicopathological diagnosis. Bias was also minimized by setting the same parameters for image acquisition and image analysis for all cases.

QUANTIFICATION AND STATISTICAL ANALYSIS

Differences in age and PMI were assessed using Kruskal-Wallis and one-way ANOVA, respectively. Distributions of data were examined using histograms and Shapiro-Wilks tests. The majority of statistical analyses used mixed effect models (*lmerTest* package in R) to investigate the effect of disease status, *APOE* and sex on the variable of interest, while controlling for potentially confounding variables and specifying the random effect to account for repeated measures. Models were generated and residuals assessed. If data failed to meet model assumptions data was transformed using Tukey or Box-Cox transformations.

After running the mixed effects model, an ANOVA (*stats* package — Type III Analysis of Variance Table with Satterthwaite's method) was performed on the model output to determine the main and interaction effects. If the interaction was significant or if the main effect was significant and had more than 2 levels, the *emmeans* package was used to compute multiple comparisons, where the Kenward-Rogers method for degrees of freedom and the Tukey method for p value adjustment were employed.

Correlations used Pearson's of Spearman's methods, dependent on whether data met assumptions for parametric testing or not.

Statistical significance was set at 5% ($\alpha = 0.05$). Statistical details can be found in the figure legends and results text, including the statistical tests used, exact value of n, what n represents, and dispersion and precision measures.

All the analyses were performed with R[80] and the scripts and full statistical results can be found at https://doi.org/10.7488/ds/3837.

Neuron, Volume *111*

Supplemental information

Synaptic oligomeric tau

in Alzheimer's disease — A potential culprit

in the spread of tau pathology through the brain

Martí Colom-Cadena, Caitlin Davies, Sònia Sirisi, Ji-Eun Lee, Elizabeth M. Simzer, Makis Tzioras, Marta Querol-Vilaseca, Érika Sánchez-Aced, Ya Yin Chang, Kristjan Holt, Robert I. McGeachan, Jamie Rose, Jane Tulloch, Lewis Wilkins, Colin Smith, Teodora Andrian, Olivia Belbin, Sílvia Pujals, Mathew H. Horrocks, Alberto Lleó, and Tara L. Spires-Jones

Supplementary material

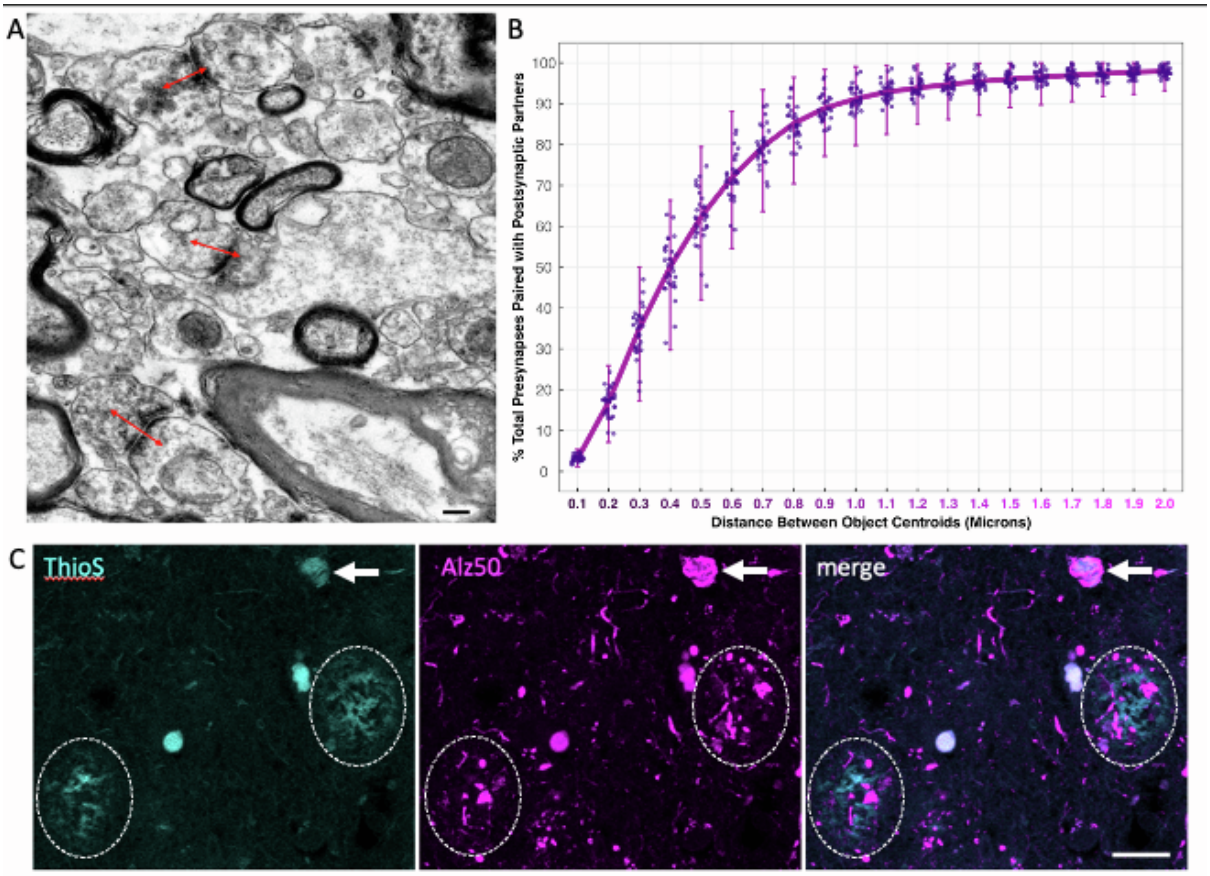

Figure S1. Synaptic pairs and identifying pathological lesions. Related to Figure 1. Synaptic pairs in array tomography were defined as pre and post-synaptic puncta with centroids within 500 nm (0.5 μm). This is based on electron microscopy data (example in panel **A**) showing that the centre of presynaptic terminal staining is within 500nm of the PSD of the majority of synapses (red arrows 500nm in length). Further this cut-off in our array tomography data results in 60% of presynaptic terminals having a postsynaptic partner (**B**). This is lower than the expected 80-90% excitatory synapses but reduces the chances of counting false positives which is important for inferring trans-synaptic tau spread in this study. In the array tomography study, synapse density was assessed in proximity to Alz50 positive neurofibrillary tangle pathology or neuritic plaques defined by Alz50 positive dystrophic neurite patterns. To confirm these patterns of dystrophic neurites are indeed neuritic plaques, we used confocal imaging of paraffin sections stained with thioflavin S to label plaque and tangle fibrils and Alz50 immunohistochemistry and confirmed that Alz50 labels tangles (**C**, arrows) and that Alz50 positive dystrophic neurite surround ThioS positive plaques (**C**, circles). Scale bars represent 500nm in A, 20 μm in **C**.

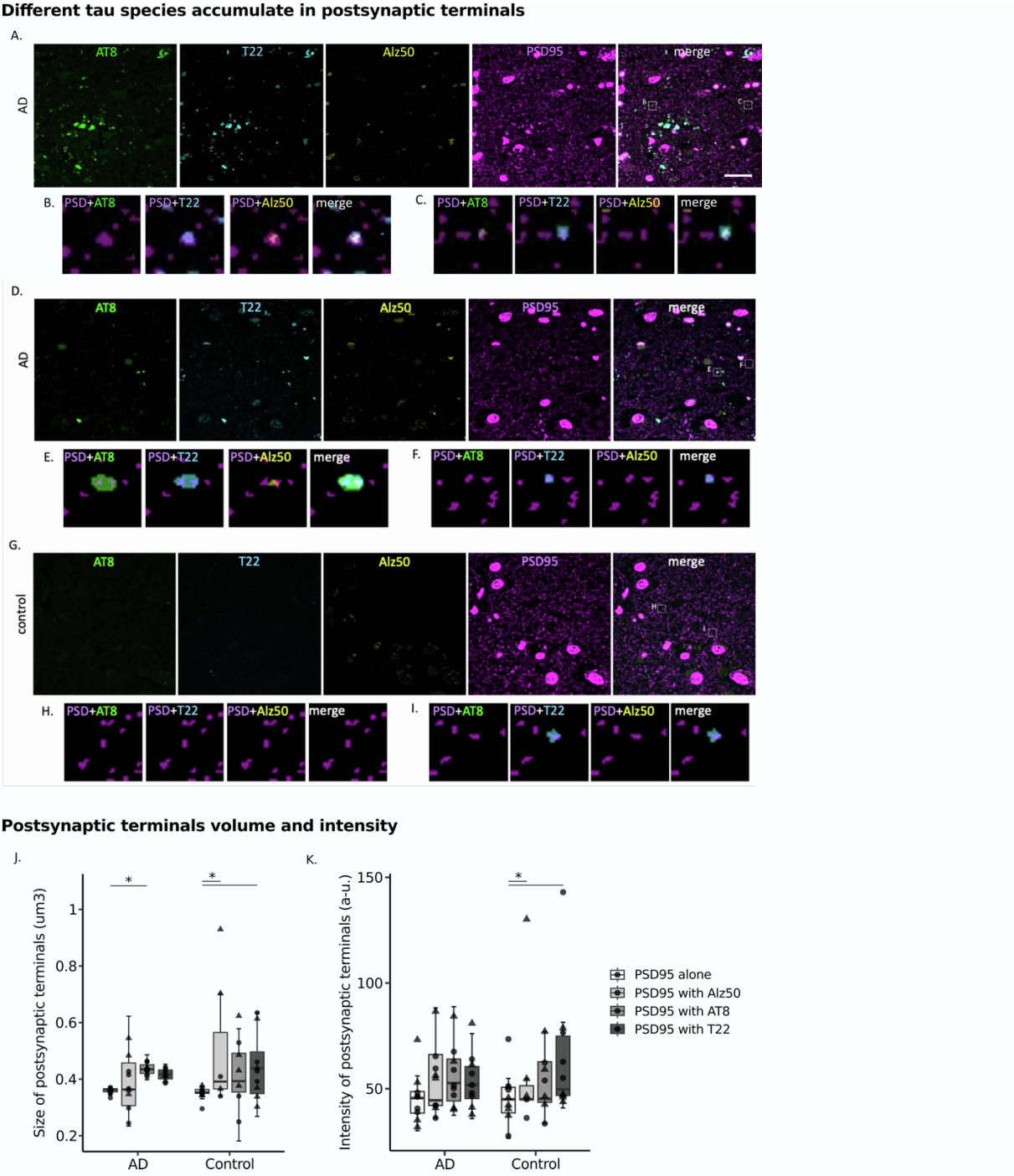

Figure S2. Different tau species accumulate in postsynaptic terminals. Related to Figure 2. Top panel shows three more examples of postsynaptic terminals containing tau **A., D** and **G** shows a single 70nm-thick section from two AD and a control case stained with oligomeric tau (T22, cyan), misfolded tau (Alz50, yellow) and Ser202, Thr205 phosphorylated tau (AT8, green) and postsynaptic (PSD95, magenta). All three types of tau can be observed in postsynapses as shown in 5umx5um insets below (**B, C, E, F, H, I**). **Bottom panel** shows quantification of postsynaptic terminals volume and intensity in relation to tau species present**.** In **A** are plotted the size of PSD95 puncta in AD and control cases depending on the presence of tau species. In **B** are plotted the mean signal intensity of postsynaptic terminals in AD and control cases in relation to the presence of tau species. Boxplots show quartiles and medians calculated from each image stack. Data points refer to case means (females, triangles; males, circles). Analysis was with linear mixed effects models including diagnostic group, sex and tau specie presence. *p<0.05 in post-hoc emmeans test after linear mixed effects model. Abbreviations: a.u., arbitrary units. Scale bars represent 20 μm.

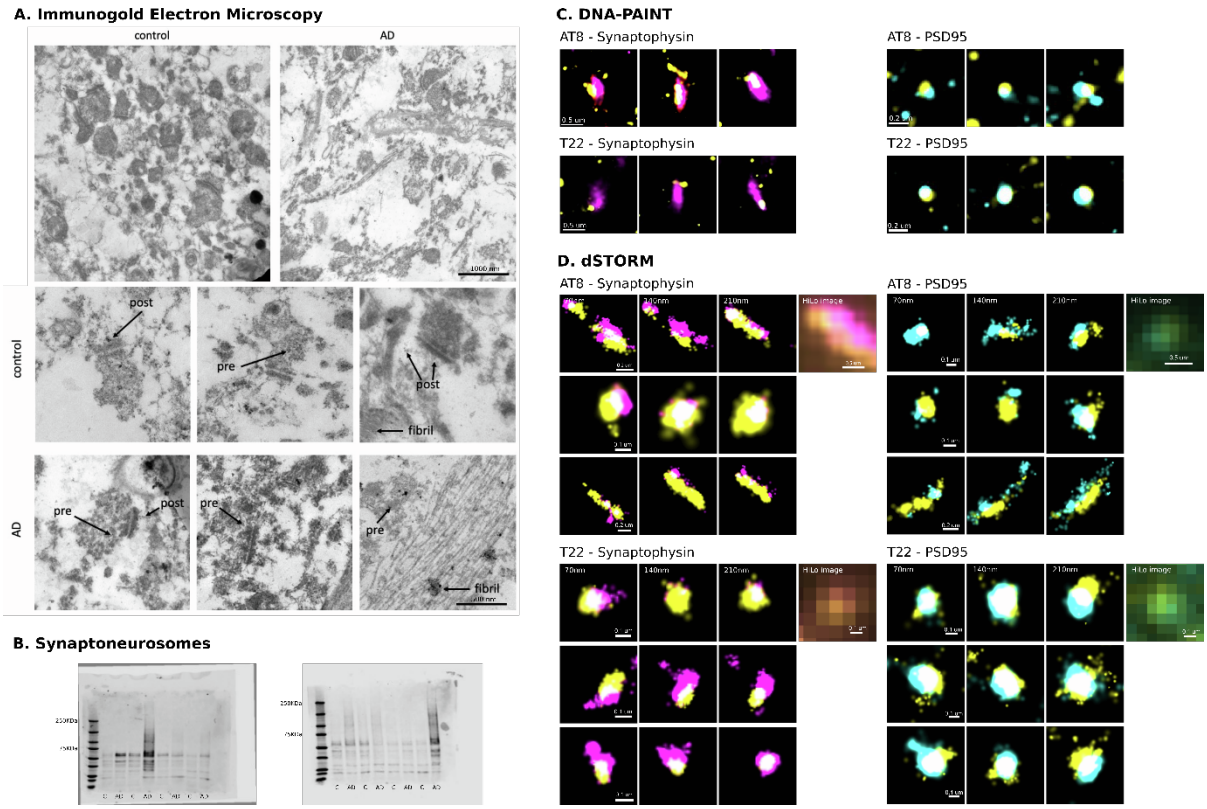

Figure S3. Confirmation of AD synaptic tau aggregates. Related to Figure 3. **A** Immuno-electron microscopy with gold-conjugated secondary antibodies (black dots) shows T22 at pre- and postsynaptic terminals. Scale bar top = 1000nm bottom = 500nm. **B** Full western blots from synaptoneurosomes isolated from 8 control and 8 AD cases. **C** Examples of DNA-PAINT array tomography 70nm-thick sections confirm tau (yellow) and synaptophysin (magenta) or PSD95 (cyan) colocalization. **D** Examples of dSTORM array tomography 70nm-thick consecutive sections confirm tau (yellow) and synaptophysin (magenta) or PSD95 (cyan) colocalization after reconstruction of HiLo images.

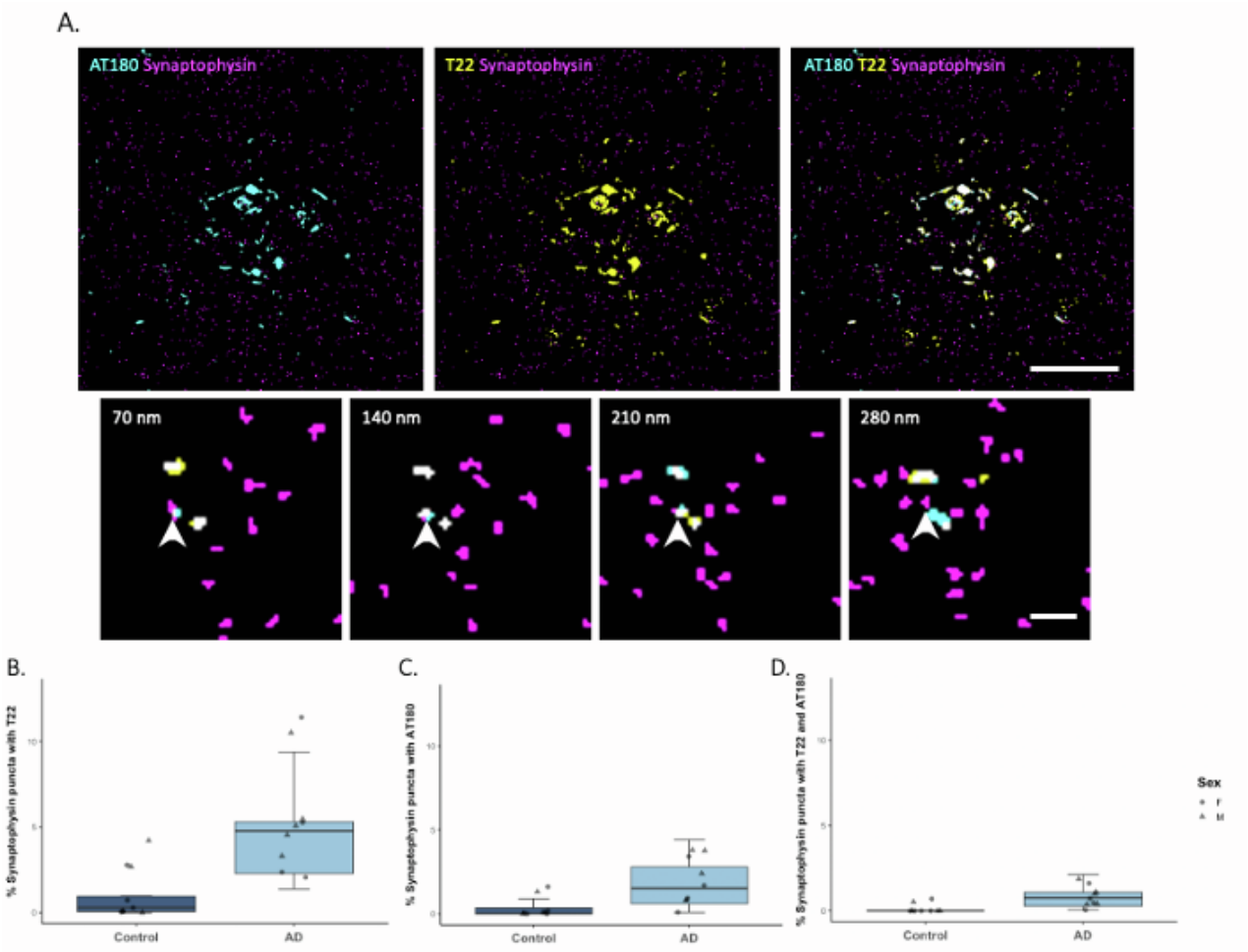

Supplementary Figure 4. Oligomeric tau is more prevalent than an early phosphoepitope in presynaptic terminals in AD cases. Related to Figure 4. A At top, maximum intensity projection of a representative segmented image from array tomography showing presynaptic terminals (magenta), ptau231 (AT180, cyan) and/or oligomeric tau (T22, yellow). The inset below shows four consecutive 70nm thick sections where a presynaptic terminal containing both tau species is pointed by an arrowhead. **B** Percent of presynaptic terminals containing oligomeric tau (T22). **C** Percent of presynaptic terminals containing ptau231 (AT180 clone). **D** Percent of presynaptic terminals containing both oligomeric and ptau231 . Boxplots show quartiles and medians calculated from each image stack. Data points refer to case means (females, circles; males, triangles). Analysis was with linear mixed effects models including diagnostic group and sex. Scale bars represent 20 μm and 2 μm.

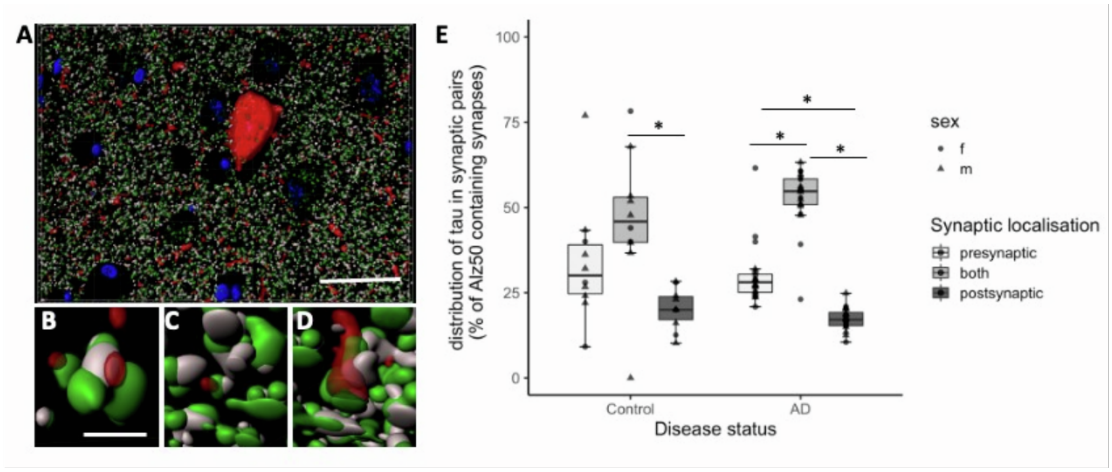

F

MouseID	Genotype	Age (months)	Sex
78181	rTgTauEC + EC-tdTomato/Syp-GFP	3	f
78184	rTgTauEC + EC-tdTomato/Syp-GFP	3	f
78192	rTgTauEC + EC-tdTomato/Syp-GFP	3	f
74759	rTgTauEC + EC-tdTomato/Syp-GFP	9	m
74767	rTgTauEC + EC-tdTomato/Syp-GFP	9	m
74788	rTgTauEC + EC-tdTomato/Syp-GFP	9	m
74818	rTgTauEC + EC-tdTomato/Syp-GFP	9	f
73177	rTgTauEC + EC-tdTomato/Syp-GFP	18	m
73154	rTgTauEC + EC-tdTomato/Syp-GFP	18	f
73140	rTgTauEC + EC-tdTomato/Syp-GFP	18	m
73132	EC-tdTomato/Syp-GFP (control)	18	m

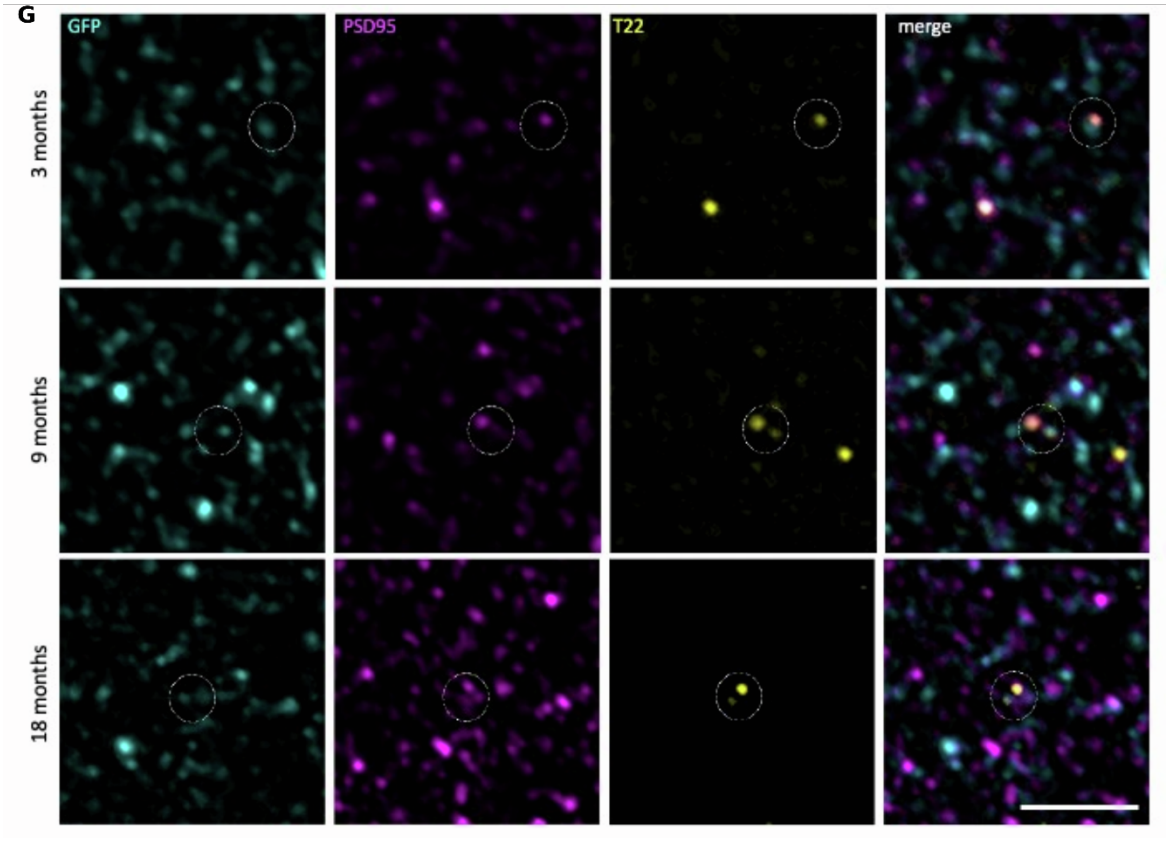

Supplementary Figure 5. Tau distribution at synaptic terminals. Related to Figure 5. Panel **A** Shows a 3D reconstruction made in Imaris of array tomography images of misfolded tau (Alz50, red), presynaptic terminals (grey), post synaptic terminals (green) and DAPI (blue). We observe tau accumulation in presynaptic terminals (**B**), postsynaptic terminals (**C**) and both sides of synaptic pairs (**D**). Quantification of synaptic pairs containing tau (**E**) reveals most tau accumulation differs between presynaptic only, both sides of the pair, and postsynaptic only (ANOVA after linear model $F=62.93$, $p<0.0001$), asterisks represent post-hoc Tukey corrected tests $p<0.05$. Array tomography imaging of mice expressing P301L mutant human tau and GFP tagged synaptophysin (**F**) in entorhinal cortex stained for GFP, PSD95, and T22 (**G**) show that oligomeric tau can spread from pre to post synapses at 3 ages studied. Scale bars represent 20 μm In A, 1 μm in B-D, 5 μm in F.

Study	Technique	Antibodies	Host species	Reactivity species	Supplier	Catalogue #	Isotype	Dilution
1. Synaptic density and Alz50 localisation in BA20/21	AT	Primary						
		Synaptophysin (SY38)	Mouse	Human	Abcam	ab8049	IgG1	1:50
		PSD95 (D27E11)	Rabbit	Human	Cell Signaling Technology	3450	IgG	1:50
		Alz50	Mouse	Human	Courtesy of P. Davies		IgM	1:50
		DAPI			Sigma Aldrich	D9542		1:10000
		Secondary						
		Alexa Fluor 488®	Donkey	Rabbit	Invitrogen	A-21206	IgG	1:50
		Alexa Fluor 594®	Goat	Mouse	Invitrogen	A-21044	IgM	1:50
		Alexa Fluor 647®	Goat	Mouse	Invitrogen	A-21240	IgG1	1:50
2. Synaptic Tau species comparison in BA20/21	AT	Primary						
		PSD95	Guinnea Pig	Human	Synaptic Systems	124 014	IgG	1:50
		Tau (AT8)	Mouse	Human	ThermoFisher	MN1020	IgG1	1:50
		T22 (serum)	Rabbit	Human	Courtesy of Rakez Kayed		IgG	1:50
		Alz50	Mouse	Human	Courtesy of P. Davies		IgM	1:50
		Secondary						
		Alexa Fluor 594®	Goat	Mouse	Invitrogen	A-21044	IgM	1:50
		DyLight® 405	Goat	Mouse	BioLegend	409109	IgG1	1:50
		Cy5®	Goat	Rabbit	Abcam	ab97077	IgG	1:50
		Alexa Fluor 488®	Donkey	Guinea Pig		706-545-148	IgG	1:50
3,4,5,6 Synaptic tau confirmation in BA20/21	3. EM	Primary						
		T22 (serum)	Rabbit	Human	Courtesy of Rakez Kayed		IgG	1:50
		Secondary						
		10nm Gold	Goat	Rabbit	Abcam	ab39601	IgG	1:50
	4. dSTORM	Primary						
		Synaptophysin	Goat	Human	R&D Systems	AF5555	IgG	1:50
		Tau (AT8)	Mouse	Human	Innogenetics	90206	IgG	1:50
		T22 (purified)	Rabbit	Human	Millipore	ABN454-I	IgG	1:50
		PSD95 (D27E11)	Rabbit	Human	Cell Signaling	3450	IgG	1:50
		PSD95 (K28/43)	Mouse	Human	Neuromab	MABN68	IgG	1:10
		Secondary						
		Alexa Fluor 488®	Donkey	Rabbit	ThermoFisher	A21206	IgG	1:50
		Alexa Fluor 488®	Donkey	Mouse	ThermoFisher	A21202	IgG	1:50
		Alexa Fluor 647®	Donkey	Rabbit	ThermoFisher	A21447	IgG	1:50
		Alexa Fluor 647®	Donkey	Goat	ThermoFisher	A31573	IgG	1:50
	5. DNA-PAINT	Primary						
		Synaptophysin (YE269) - AF488	Rabbit	Human	Abcam	ab196379	IgG	1:100
		Tau (AT8)	Mouse	Human	ThermoFisher	MN1020	IgG1	1:50
		T22 (serum)	Rabbit	Human	Courtesy of Rakez Kayed		IgG	1:50
		PSD95 (D27E11)	Rabbit	Human	Cell Signaling Technology	3450	IgG	1:50
		Secondary						

		Unconjugated	Donkey	Rabbit	Invitrogen	31238	IgG	1:50
	6. WB	Primary						
		Tau5	Mouse	Human	BioLegend	806401	IgG	1:250
		GAPDH	Rabbit	Human	Cell Signaling	2118	IgG	1:1000
		B-actin	Mouse	Human	Cell Signaling	3700	IgG	1:1000
		VAMP2	Rabbit	Human	Cell Signaling	13508	IgG	1:1000
		Secondary						
		Goat anti-Rabbit IR Dye 800	Goat	Rabbit	Li-COR BioSciences	926-32211	IgG	1:5000
		Goat anti-Mouse IR Dye 700	Goat	Mouse	Li-COR BioSciences	926-32220	IgG	1:5000
7. Tau pathology burdens in BA20/21 and BA17	IHC	Primary						
		Tau (AT8)	Mouse	Human	ThermoFisher	MN1020	IgG1	1:850
		Secondary Antibodies						
		Novolink Polymer Detection System		Mouse	Leica Biosystems	RE7200		
8. Synaptic oligomeric tau in BA20/21 and BA17	AT	Primary						
		Synaptophysin (YE269) - AF488	Rabbit	Human	Abcam	ab196379	IgG	1:100
		PSD95 (K28/43)	Mouse	Human	DSHB	K28/43	IgG2 A	1:50
		T22 (serum)	Rabbit	Human	Courtesy of Rakez Kayed		IgG	1:50
		DAPI			Sigma Aldrich	D9542		1:10000
		Secondary						
		Cy3®	Donkey	Mouse	Jackson Immuno	715-165-150	IgG	1:50
		Cy5®	Donkey	Rabbit	Jackson Immuno	711-175-152	IgG	1:50
9. Synaptic pTau231 and oligomeric tau in BA20/21	AT	Primary						
		AT180	Mouse	Human	ThermoFisher	MN1040	IgG1	1:50
		T22 (serum)	Rabbit	Human	Courtesy of Rakez Kayed		IgG	1:50
		Synaptophysin (YE269) - AF488	Rabbit	Human	Abcam	ab196379	IgG	1:50
		Secondary						
		DyLight® 405	Donkey	Mouse	Abcam	Ab175658	IgG1	1:50
		Alexa Fluor 594®	Donkey	Rabbit	ThermoFisher	A21207	IgG	1:25
10. Mouse array tomography study	AT	Primary						
		PSD95	Guinea Pig	Mouse, human	Synaptic Systems	124014	IgG	1:50
		T22 (serum)	Rabbit	Human	Courtesy of Rakez Kayed		IgG	1:25
		GFP	Chicken	jellyfish	Aves labs	GFP-1020	IgY	1:50
		Secondary						
		Alexa Fluor 647®	Goat	Rabbit	ThermoFisher	A21244	IgG	1:50
		Alexa Fluor 488®	Goat	Chicken	ThermoFisher	A11039	IgY	1:50
		Alexa Fluor 594®	Goat	Guinea Pig	ThermoFisher	A11076	IgG	1:50

Table S1 – Antibody combinations by experiment. Related to Table 1 and STAR methods. AT: Array tomography microscopy. EM: Immunogold electron microscopy. dSTORM: Direct Stochastic Optical Reconstruction Microscopy. WB: Western blot. IHC: Immunohistochemistry.